Direct Numerical Simulation of Physiological Pulsatile Flow through Arterial Stenosis

by

Md. Abul Khair

A Thesis submitted to the Faculty of Graduate Studies of

The University of Manitoba

in partial fulfilment of the requirements of the degree of

MASTER OF SCIENCE

Department of Mechanical & Manufacturing Engineering

University of Manitoba

Winnipeg

Abstract

In this research, pulsatile blood flow through a modeled arterial stenosis assuming Newtonian and non-Newtonian viscous behavior is simulated using direct numerical simulation (DNS). A serial FORTRAN code has been parallelized using OpenMP to perform DNS based on available high performance shared memory parallel computing facilities. Numerical simulations have been conducted in the context of a channel with varying the degree of stenosis ranging from 50% to 75%. For the pulsatile flow studied, the Womersley number is set to 10.5 and Reynolds number varies from 500 to 2000, which are characteristic of human arterial blood flows. In the region upstream of the stenosis, the flow pattern is primarily laminar. Immediately after the stenosis, the flow recirculates and an adverse streamwise pressure gradient exists near the walls and the flow becomes turbulent. In the region far downstream of the stenosis, the flow is re-laminarized for both Newtonian and non-Newtonian flows.

Acknowledgements

First of all, I would like to express my sincere thanks to my supervisors, Dr. Bing-Chen Wang and Dr. David C. S. Kuhn, for their invaluable help and steadfast support throughout the period of this research. I am also thankful to them for their wise criticisms and suggestions in preparing and improving of this thesis. I wish to thank Western Canada Research Grid (WestGrid) for the opportunity to use the high performance computing facilities.

My sincere thanks also go to Dr. M. F. Tachie and Dr. S. J. Ormiston for their advice during my course studies. I would like to thank Afzal Hossain and Dr. Mamun Molla for their suggestions and help during my study. I also like to thank all my friends for their encouragements during this research. Many thanks to Mohammad Saeedi and Iman Fatemi with whom I shared my office room and from whom I learned many things.

I am grateful to my beloved parents, brothers and sisters, whose love is more than I can desire. I am also grateful to all of my well-wishers for their inspiration that leads me to complete this thesis.

To my parents

Table of Contents

List of Figures

Nomenclature

English Symbols

A	Amplitude of the pulsatile oscillations
$\mathbf{A}$, A_{kj}	Cofactor matrix and tensor
E	Energy spectrum
f	Flow variable
f_c	Parameter for controlling the height of the stenosis: δ/h
f_{par}	Parallel fraction of the code
f_s	Time frequency of eddy motions
h, δ	Height of the channel (h is a constant and $\delta = \delta(x)$ is a variable)
i	Imaginary unit: $\sqrt{-1}$
$\mathbf{J}$	Jacobian of the cofactor matrix
k	Turbulence kinetic energy
l	Integral length scale
M_n	Coefficient
N	Number of the pulsatile cycles
N_{xyz}	Number of grid nodes
P	Number of processors
p	Pressure
Re	Reynolds number: $\frac{Uh}{\nu}$
Re_T	Turbulent Reynolds number
S	Speedup
Sr	Strouhal number
s_{ij}	Strain rate tensor

t	Time
t_0	Initial time
T	Time period of a pulsatile cycle
T_1	Execution time of an application on 1 processor
T_p	Execution time of an application on P processors
u_0	Velocity scale
u_i	Velocity components
u, v, w	Velocity components (corresponding to u_1, u_2, u_3, respectively)
U	Bulk velocity
U_c	Mean convective velocity at the outlet
x, y, z	Coordinates of a Cartesian frame

Greek Symbols

α	Womersley number: $\left(h^2\frac{\omega}{\nu}\right)^{\frac{1}{2}}$
δ_{ij}	Kronecker delta
ϵ	Dissipation rate
η_l	Kolmogorov length scale: $\left(\frac{\nu^3}{\epsilon}\right)^{\frac{1}{4}}$
η_t	Kolmogorov time scale: $\left(\frac{\nu}{\epsilon}\right)^{\frac{1}{2}}$
ϕ_n	Phase angle
μ	Molecular dynamic viscosity of the fluid
ν	Molecular kinematic viscosity of the fluid
ω	Frequency: $2\pi/T$
ρ	Fluid density
τ_w	Wall shear stress
ξ_k	Curvilinear coordinates

Subscripts and Superscripts

$(\,)_{reatt}$	Point of reattachment
$(\,)_{sep}$	Point of separation
$\langle\,\rangle$	Time- and spanwise-averaged quantity

Abbreviations

2D	2-Dimensional
3D	3-Dimensional
API	Application Programming Interface
CFD	Computational Fluid Dynamics
CV	Control Volume
CY	Carreau-Yasuda
DNS	Direct Numerical Simulation
FFT	Fast Fourier Transform
LDV	Laser Doppler Velocimetry
LES	Large-eddy Simulations
MPI	Message Passing Interface
OpenMP	Open Multi-Processing
PIV	Particle Image Velocimetry
RANS	Reynolds-Averaged Navier-Stokes Method
RMS	Root-Mean-Square
SMP	Symmetric Multi-Processor
TKE	Turbulence Kinetic Energy
WSS	Wall Shear Stress

Chapter 1

Introduction

1.1 Background

Blood flow through arteries is pulsatile and can be laminar, turbulent or transitional depending upon the diameter, tortuosity and geometry of the blood vessels. Vascular disease adds complexity to the vascular geometry and can cause significant narrowing (stenosis) or expansion (aneurysm) of large arteries that may lead to laminar-turbulent transitional flow. Arterial stenosis is commonly found in patients who have vascular disease. It is generally caused by atherosclerosis where cholesterol and other lipids are deposited beneath the intima (inner lining) of the arterial wall, and can occur acutely as a result of emboli or trauma. There is often an accompanying proliferation of connective tissue which forms a thickened area in the vessel wall called plaque as the amount of the fatty material increases. The vessel wall remodels to accommodate this condition to varying degrees, but with marked plaque deposition, the effective cross-section of the vessel reduces and retards blood flow. Furthermore, blood flow may transit to turbulence and its pressure typically drops in the vessel section immediately downstream of the stenosis. The alteration in flow dynamics in turn produces abnormal wall shear stress both at the plaque and at the post-stenotic region. Once the surface of the stenosis is damaged, it might form a blood clot that retards blood flow in a cerebral artery or in a coronary artery. Moreover, blood may stagnate in the post-stenotic region and form a blood clot that may be transferred to the lung (Ku [2]).

With the need for deeper insights into the physics of flows through arterial stenoses and the advancement of computation technology, the past decade has witnessed a rapid advancement in numerical simulation of physiological pulsatile flows through different types of stenoses. To date, the method of DNS has been applied to several numerical investigations of transitional pulsatile flow (Varghese *et al.* [3,4], Bhaganagar [5], Paul and Molla [6]). The computational cost involved in a DNS approach is typically demanding, as both the temporal and spatial scales of turbulence need to be fully resolved (including the smallest Kolmogorov scales). Nevertheless, DNS has the potential to be the most useful tool for numerical investigation of physiological pulsatile blood flow through arteries as the Reynolds number is typically low in human arteries [2].

1.2 Newtonian Flow in Stenosis Studies

There are many challenges involved in numerical modeling of blood flows. The geometry of a stenosis in a blood vessel can be highly irregular and the boundary material can be nonlinear and elastic, complex physiological conditions such as pulsations can be involved, and the behavior of the blood fluid itself can be Newtonian in large arteries and non-Newtonian in small arteries (Molla *et al.* [7]). In order to study the physical mechanisms of pulsatile Newtonian blood flows through stenoses, several experiments have been conducted to investigate the flow pattern and the shear stresses at the walls under steady and pulsatile flow conditions. Khalifa and Giddens [8, 9] studied the evolution of post-stenotic flow disturbances using laser Doppler velocimetry (LDV). Their experimental investigation of the velocity field was performed along the central streamline of a plexiglass tube. The Reynolds number and the Womersley number were chosen 600 and 7.6, respectively. Here, the Reynolds number is defined as $Re \stackrel{\text{def}}{=} \frac{Uh}{\nu}$, where U is the bulk velocity and ν is the kinematic viscosity of the fluid. The Womersley number α is defined as $\alpha^2 \stackrel{\text{def}}{=} h^2 \frac{\rho\omega}{\mu}$, where ρ is the density of the fluid, μ is dynamic viscosity of the fluid, $\omega = \frac{2\pi}{T}$ is the frequency of the pulsations, and T is the time period a pulsation cycle. The Womersley number

reflects the ratio of the pulsatile inertial forces to the viscous forces. In their research, Khalifa and Giddens [8, 9] systematically studied a periodic disturbance arising from the shear layer due to pulsations, coherent structures associated with the initiation of each pulsatile cycle, and characteristics of the statistically non-stationary turbulence created by the stenosis.

Peterson and Plesniak [10] conducted an experiment using LDV and particle image velocimetry (PIV) to determine the influence of two physiologically relevant inlet conditions on the flow physics downstream of an idealized stenosis. The test case was run for a stenosis of 75% with mean Reynolds number of 364 and a Womersley number of 4.6. The two inlet conditions included an asymmetric mean inlet velocity profile and an asymmetric mean inlet velocity profile superimposed with a secondary flow as found downstream of a bend. They found that the asymmetric inlet velocity profile reduced the influence of stenosis by forcing the stenotic jet towards the tube wall through an induced non-uniform radial pressure gradient, however, the vortex ring formation was relatively unaffected by the mean velocity gradient and secondary flow.

Ahmed and Giddens [11, 12] investigated flow disturbances through an axisymmetric stenosis formed within a rigid tube. They used LDV and a flow visualization technique to study a stenotic flow with Reynolds numbers ranging from 500 to 2000. However, the inlet boundary condition in their study was steady, which does not reflect the pulsatile nature of blood flow in arteries. They reported that the flow field transitioned to turbulence when $Re \geq 1000$ and the maximum streamwise velocity occurs at the centre of the stenosis. The length of the recirculation zone (distance from the stenosis to reattachment point) was shorter at $Re = 2000$ than $Re = 1000$.

Ahmed and Giddens [13] further investigated the post-stenotic flow behavior using sinusoidal pulsatile inflow conditions based on a Reynolds number fixed to 600 and Womersley numbers ranging from 7.5 to 15. They concluded that under the pulsatile inflow condition tested, even a mild stenosis can lead to transition to turbulent flow in the post-stenotic region. Cassanova and Giddens [14] also made a similar

conclusion based on their case for Reynolds numbers ranging from 318 to 2540 and Womersley number fixed to 15. Ahmed [15] re-investigated the pulsatile flow through a smooth constriction using a two-dimensional (2D) LDV. He conducted experiments at a Reynolds number of 600 and stenoses of 25%, 50% and 75% degree of contraction. Ahmed [15]found that different types of flow disturbances exist downstream of the stenosis and they were sensitive to the geometry of stenosis. During the acceleration phase of the pulse, the average disturbance level was relatively low. At the peak phase, the highest disturbance level was observed. The disturbance level decreases significantly during the deceleration phase. The results presented by Ahmed [15] on post-stenotic turbulent flow physics are similar to those of Yongchareon and Young [16].

As discussed above, the fluid dynamics of post-stenotic blood flow plays a crucial role in the diagnosis of arterial disease. So, there is considerable interest in gaining better insight into the dynamics of post-stenotic flows. Computational fluid dynamics (CFD) is one of the most popular tools for gaining accurate results and visualizing the flow field. Several studies have been reported which provide insights into the physical mechanisms underlying transition-to-turbulent flows through arterial stenoses. Early studies of pulsatile laminar flow through the model arterial stenosis were represented by Cheng *et al.* [17], Daly [18] and O'Brien and Ehrlich [19]. Cheng *et al.* [17] investigated a pulsatile flow through a channel with a square shaped stenosis, and Daly [18] and O'Brien and Ehrlich [19] used an axisymmetric cosine shape stenosis. Daly [18] used physiological pulsatile flow at the inlet whereas a simple sinusoidal pulsatile flow was considered by Cheng *et al.* [17] and O'Brien and Ehrlich [19]. In their findings, Cheng *et al.* [17] and Daly [18] concluded that the pressure gradient and the shear stress drops are maximum at the throat of the stenosis. On the other hand, O'Brien and Ehrlich [19] found that the peak wall vorticity occurred just prior to the centre of the stenosis and is proportional to the wall shear stress.

A steady state flow through an axisymmetric stenosis has been investigated extensively by Smith [20] using an analytical approach which indicates that the flow patterns strongly depend upon the geometry of the stenosis and upstream Reynolds

number. Smith [20] concluded that under the conditions of moderately severe and very severe constrictions and even under any slowly varying constrictions, the major separation occurs near the maximum constriction point. Since the pulsatile nature of the flow is fundamentally important, many theoretical and experimental studies of stenotic flows have been conducted, which include the early influential work of Imaeda and Goodman [21], Tu *et al.* [22], and Zendehbudi and Moayeri [23]. Haldar [24] dealt with the problem of oscillatory blood flow through a rigid tube with mild constriction under a simple harmonic pressure gradient and examined the effect of stenosis on the flow field.

Varghese and Frankel [25], Lee *et al.* [26, 27] and Li *et al.* [28] studied 2D laminar-turbulent transitional flows passing an arterial stenosis using a Reynolds-averaged Navier-Stokes (RANS) approach based on the k-ω turbulence models. Scotti and Piomelli [29] later indicated that the RANS turbulence models have some limitations in modeling pulsatile flows where the inlet velocity profile and pressure gradient oscillate with time. They found that although the RANS models gave good predictions of mean velocity profiles, their predictions of higher-order turbulence statistics such as the Reynolds shear stresses, turbulent kinetic energy and dissipation rate may not be entirely satisfactory. Furthermore, these RANS models are not capable of simulating instantaneous pulsatile turbulent flows as the governing equations of the RANS approach are ensemble-averaged.

Stroud *et al.* [30] investigated the influence of stenosis on pulsatile laminar flow through stenotic vessels with the Reynolds number ranging from 200 to 1200, whereas Melaaen [31] studied the steady flow in a constricted tube for $Re = 200$. Based on analysis of the results for degree of stenosis 25%, 50% and 75%, Stroud *et al.* [30] found that surface irregularity, stenosis aspect ratio, and the pulsatile waveform have considerable influence on the flow field and on the wall shear stresses on the plaque deposits. Bertolotti and Deplano [32] analyzed the steady flow pattern for a stenosed coronary bypass for $Re = 250$ with and without a 75% severity stenosis for three different locations. They observed that two counter-rotating structures formed in crossplanes downstream from the junction and a short area of negative wall shear

stress developed just after the stenosis.

Dvinsky and Ojha [33] simulated sinusoidal pulsatile laminar flow through an asymmetric stenosis. Long *et al.* [34] investigated physiological pulsatile laminar flow through an axisymmetric arterial stenosis with a Reynolds number of 300. Dvinsky and Ojha [33] considered a cosine-shaped asymmetric stenosis, whereas in Long *et al.* [34], the shape of the stenosis was approximated by two integrated Gaussian functions at the proximal and distal ends together with a straight segment in between. Long *et al.* [34] found that the formation and development of flow separation zones in the post-stenotic region are very complex, especially during the flow deceleration phase. They also observed that the flow relaminarizes and becomes fully-developed earlier for the asymmetric cases than for the axisymmetric cases.

Varghese *et al.* [3, 4] investigated both pulsatile and non-pulsatile flows in the context of symmetric and eccentric stenoses using the DNS approach. They analyzed turbulence statistics downstream of an eccentric stenosis at a relatively low Reynolds number of 300. For such a low Reynolds number, flow transits from laminar to turbulent and the shear stress oscillates highly in the post-stenotic region. Sherwin and Blackburn [35] and Blackburn and Sherwin [36] studied three-dimensional (3D) instabilities and transition of pulsatile flows in a stenotic tube using DNS based on the spectral method. For their pulsatile test case, they used simple sinusoidal pulses with the flow Reynolds number ranging from 250 to 800. They found that after a linear instability phase, vortex rings were ejected from the stenosis, which rapidly broke down into finer-scale components. Furthermore, they observed that this characteristic was similar to the final state of the non-pulsatile flow, however, the instability and transition mechanisms are very different and occur at a lower Reynolds number.

1.3 Non-Newtonian Flow in Stenosis Studies

The assumption of the Newtonian behavior of blood is pertinent for high shear rate flow through large arteries. Meanwhile, it has been confirmed by experiments that

blood behaves as a non-Newtonian fluid at low shear rates and in vessels of small diameters (Mann and Tarbell [37], Ku [2]), exhibiting marked shear thinning and significant viscoelastic properties under pulsations (Phillips and Detsch [38]). Since the shear rate is low on the downstream side of a stenosis, a correct analysis of the flow pattern should also include the shear-thinning characteristics of blood. Mann and Tarbell [37] experimentally studied the influence of non-Newtonian rheology on wall shear rates in steady and oscillatory flows through rigid curved and straight artery models. They used four fluids: aqueous glycerin (Newtonian), aqueous polyacrylamide (shear thinning and highly elastic), aqueous Xanthan gum (shear thinning and moderately elastic), and bovine blood. They concluded that for steady flow conditions, there was little difference in the wall shear rate levels measured for the four fluids. They also concluded that polyacylamide is too elastic to provide a good model of blood flow under oscillatory conditions, particularly when there is wall shear reversal.

Box *et al.* [39] investigated the effects of non-Newtonian blood viscosity, variations in flow rate, and vessel diameter on near-wall flow behavior in a carotid bifurcation vessel model. The blood viscosity is a function of shear rate, and was calculated using the Carreau-Yasuda (CY) model. They found that the CY model gave a good approximation of the viscosity of blood in the shear rate range from 375 to 750 s^{-1} and maximum wall shear stresses oscillations occurred at the edges of the recirculation region in a carotid bifurcation. Later, Boyd *et al.* [40] utilized the Casson and CY non-Newtonian blood viscosity models to simulate 2D Newtonian and non-Newtonian flows in the context of a simple steady flow and an oscillatory flow in straight and curved pipes. They observed that in the steady flow case, both the Casson and CY models show large differences in the predicted velocity profiles in comparison with corresponding Newtonian flow velocity profile. It is found that in steady and pulsatile conditions, the Casson model produced the largest variations from Newtonian flow behaviors.

Choi and Barakat [41] performed numerical simulations of steady and pulsatile Newtonian and non-Newtonian flows over a backward facing step. The shear-thinning

model of Carreau [42] was used for predicting non-Newtonian flows. They observed that for the pulsatile flow case, the shear stress within the flow recirculation zone was significantly larger for the Newtonian fluid than for the non-Newtonian fluid. Nakamura *et al.* [43] studied a non-Newtonian blood flow through an axisymmetric stenosis model. They suggested that the axial force acting on the stenosis can become one of the causes for post-stenotic dilatation. They also found that the non-Newtonian assumption of blood weakens the distortion of flow pattern, pressure and shear stress at the wall associated with the stenosis. However, they did not study the effect of pulsation on the flow.

Ishikawa *et al.* [44] performed numerical simulations of the pulsatile non-Newtonian flows through an arterial stenosis using the bi-viscosity model for blood. They found that the non-Newtonian effects reduced the strength of the vortex downstream of the stenosis. However, the study was limited to mild stenosis of severity less than 50%. In their extensive study, Easthope and Brooks [45] found that the Walburn and Schneck model [46], which can degenerate to the familiar Power-law relationship for the non-Newtonian flow, is highly effective modeling blood flow within the shear rate range from 0.03 to $120s^{-1}$. Later, Hron *et al.* [47] investigated pulsatile flows of a power-law fluid in the presence of stenosis using the FEATFLOW solver. They conducted simulations at Reynolds numbers of 1000 and stenosis of 50%. Hron *et al.* [47] observed a dramatic variation of the wall shear stress in the region of the stenosis in time and in axial distance.

DNS has only recently been applied to the study of physiological transitional flow in bio-fluid mechanics. In this research DNS will be applied to simulation of physiological pulsatile transitional non-Newtonian blood flow with stenosis 60%. It has great interest to compare the results of Newtonian and non-Newtonian fluids in a model stenosis. There is an interest for further investigation using DNS in a physiological pulsatile flow through model arterial stenosis for high Reynolds number with varying degrees of stenosis. Moreover, 3D simulation of such test cases with DNS can provide in-depth information of physiological pulsatile blood flow through arteries.

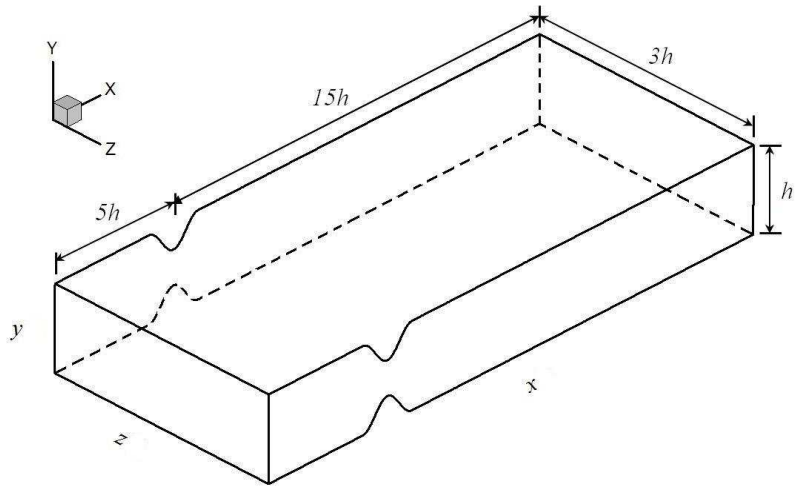

FIGURE 1.1: Schematic of an idealized symmetric stenosis model and associated coordinate system.

1.4 Objective of the Thesis

In this research, physiological pulsatile flows through a 3D stenotic channel with two-sided constrictions are studied numerically using DNS. The Newtonian and non-Newtonian effects on physiological pulsatile flows will be analyzed. An in-house computer code based on curvilinear Cartesian coordinates is used to conduct the unsteady numerical simulations on the public-domain supercomputer network WestGrid. The objectives of this research are:

- Parallelize an existing serial FORTRAN code using OpenMP to reduce code execution time. The serial FORTRAN code is a revised version of the LES-BOFFIN code, a computer code originally developed by Jones *et al.* [48, 49] for conducting large-eddy simulations (LES).

- Characterize and compare physiological pulsatile Newtonian and non-Newtonian flows through a 3D stenotic channel using DNS. The test case is shown in Fig. 1.1.

- Validate DNS results with experimental data in order to examine the predictive accuracy of the numerical approach.

Chapter 2

Numerical Method

2.1 Governing Equations

The Navier-Stokes equations of motion are suitable for use in investigating the flow physics of blood through the arterial stenosis. It is assumed that the fluid is homogeneous and incompressible. In DNS, the continuity and momentum equations for a homogeneous incompressible flow take the following forms in a general Cartesian curvilinear coordinate system

$$\frac{A_{kj}}{|\mathbf{J}|}\frac{\partial u_j}{\partial \xi_k} = 0 \tag{2.1}$$

$$\frac{\partial u_i}{\partial t} + \frac{A_{kj}}{|\mathbf{J}|}\frac{\partial u_i u_j}{\partial \xi_k} = -\frac{A_{ki}}{\rho|\mathbf{J}|}\frac{\partial p}{\partial \xi_k} + \nu\frac{A_{kj}}{|\mathbf{J}|}\frac{\partial}{\partial \xi_k}\left(\frac{A_{lj}}{|\mathbf{J}|}\frac{\partial u_i}{\partial \xi_l}\right) \tag{2.2}$$

In the above equations, A_{kj} are the elements of the cofactor matrix, $\mathbf{A}$, of the Jacobian $|\mathbf{J}|$. Cartesian tensor notation is used in the above equations, where x_j is the coordinate system and u_j is the corresponding velocity components, p is the pressure, ρ is the density and ν is the kinematic viscosity of the fluid.

The above equations describe the physics of incompressible fluid motion under laminar as well as turbulent conditions. It is well-known that DNS of turbulent flows is still limited to relatively low Reynolds numbers owing to its high demands for computational resources. In DNS, the numerical resolution has to be fine enough to represent the dissipative scales. The enormous spatial and temporal resolution requirements resulting from this constraint for a DNS of turbulent flows have been

described by Grotzbach [50].

2.2 Direct Numerical Simulation

The most accurate approach for turbulence simulation is to solve the Navier-Stokes equations without resorting to averaging or approximation other than numerical discretization whose errors can be estimated and controlled. It is also the simplest approach from a numerical point of view. In such simulations, all of the motions of the flow are directly resolved. The computed instantaneous flow field is equivalent to a single realization of a flow obtained in a laboratory experiment. This approach is referred to as DNS.

In DNS, in order to assure that all relevant flow structures are captured, the computation domain must be large enough to include the largest eddies of the flow field. A useful measure of the latter scale is the integral scale (l) of the turbulence which is essentially the distance over which the fluctuating component of the velocity remains correlated. Thus, each linear dimension of the domain must be at least a few times the integral scale. A valid simulation must also capture all of the kinetic energy dissipation. This occurs on the smallest scales of turbulence, the ones on which the molecular viscosity is active. In view of this, the size of the grid must be no larger than a viscously determined scale, called the Kolmogorov scale, η_l.

The results of DNS contain very detailed information about the flow. This can be very useful but DNS is often too expensive to be employed in engineering practice, especially when the Reynolds number of the flow is high. DNS results are as valuable as experimental data, and often, DNS are considered as "numerical wind-tunnels and water-channels". Furthermore, in comparison with the experiments, DNS offers much more detailed information on the velocity, pressure, temperature and concentration fields, locally and instantaneously (at the smallest spatial and temporal scales of turbulent motions). DNS allows for computation of quantities that can be difficult to measure in a laboratory, e.g. an instantaneous pressure field. In DNS, it is convenient

to set up complex boundary conditions and challenging operating parameters that might be difficult or impossible to realize in a laboratory. The results of DNS can be used for assessing the predictive accuracy of turbulence models, and sometimes are even used for examining the quality of experimental data.

2.3 Resolution Requirements for DNS

To obtain an estimate for the resolution requirements for DNS of a free turbulent shear flow, Kolmogorov's first principle of similarity can be used [51]. It is assumed that the small scales of turbulence are locally isotropic, that is, the statistical properties of the small scale motions are presumed not to depend on the orientation of the coordinate system or spatial position in a sufficiently small domain within a flow for which the Reynolds number is sufficiently large. The smallest turbulent scales, dissipating the turbulent kinetic energy, are therefore presumed to be isotropic and are insensitive to any orientation that are associated with the mean flow motion and boundary geometries. Their physical properties can then only depend on the rate of dissipation, ϵ, and the kinematic viscosity, ν. Here, the TKE dissipation rate is defined as $\epsilon = 2\nu\langle s_{ij}s_{ij}\rangle$ and $s_{ij} = \frac{1}{2}(\frac{\partial u_i'}{\partial x_j} + \frac{\partial u_j'}{\partial x_i})$ is the strain rate tensor based on the instantaneous fluctuating velocities. It then follows from dimensional analysis that the smallest length and time scales in a turbulent flow are characterized by the so-called Kolmogorov length scale defined as

$$\eta_l \equiv \left(\frac{\nu^3}{\epsilon}\right)^{\frac{1}{4}} \tag{2.3}$$

and the so-called Kolmogorov time scale defined as

$$\eta_t \equiv \left(\frac{\nu}{\epsilon}\right)^{\frac{1}{2}} \tag{2.4}$$

An approximation for the TKE dissipation rate can be obtained from the large scale motion if the turbulence is locally in equilibrium, that is, if the local rate of production

of TKE equals the local rate of dissipation. The rate of TKE production, however, is determined by the large scale motions and can therefore be approximated as being proportional to the turbulent energy, $\frac{u_0^2}{2}$, and a time scale $\frac{l_0}{u_0}$, characterizing the rate at which energy is transferred from the mean motion to the turbulent fluctuations. Here u_0 is a velocity scale while l_0 is an integral length scale characterizing the large scale turbulent motions. Thus, for turbulence in local equilibrium the dissipation rate scale is

$$\epsilon \propto \frac{u_0^3}{l_0} \tag{2.5}$$

Though strictly only true for the artificial case of forced non-decaying homogeneous turbulence, this relation can be regarded as a scale relation valid for inhomogeneous turbulence as well. Available experimental evidence suggests (Tennekes and Lumley [52]) that the spectral energy transfer proceeds at a rate dictated by the kinetic energy of the large eddies, which can be approximated by $\frac{u_0^2}{2}$, and their time scale, $\frac{l_0}{u_0}$. An estimate for the Kolmogorov scales can therefore be obtained from the large scales of the problem by introducing (2.5) into (2.3).

With an approximation for the smallest turbulent length scales obtained in this manner, the computational requirements for a 3D DNS of isotropic homogeneous turbulence can be estimated. For a finite difference or finite volume method, the number of grid nodes N_{xyz}, required to resolve the large scale as well as the small scale motion in the three spatial directions, is

$$N_{xyz} \propto \left(\frac{l_0}{\eta_l}\right)^3 \propto \left(\left(\frac{l_0 u_0}{\nu}\right)^{\frac{3}{4}}\right)^3 = Re_T^{\frac{9}{4}} \tag{2.6}$$

where $Re_T = \frac{l_0 u_0}{\nu}$ is the turbulent Reynolds number of the large scale motions.

In DNS, the requirement of time accuracy over a wide range of scales does not permit very large time steps because it implies that the small scales can have large errors, which can corrupt the solution. So in order to be accurate, the integration of the solution must be done with a time step, η_t, small enough such that a fluid particle

moves only a fraction of the length scale η_l in each step, viz.

$$N_t \propto \frac{\frac{l_0}{u_0}}{\eta_t} \propto \left(\frac{l_0 u_0}{\nu}\right)^{\frac{1}{2}} \propto Re_T^{\frac{1}{2}} \tag{2.7}$$

Equation (2.6) now implies that the grid size for a DNS of homogeneous turbulence depends on the Reynolds number. As mentioned above, the scale relations represented by equations (2.3) and (2.4) indicate the requirement on the order of magnitude of spatial and temporal resolutions in a DNS. Therefore, the number of grid nodes for complex engineering type applications are expected to grow with $Re^{\frac{9}{4}}$ in flow regimes away from a solid surface. Here, Re is the flow Reynolds number which is proportional to the turbulent Reynolds number, Re_T, characterizing the large scale turbulent fluctuations. Now if the Reynolds number Re of a turbulent flow is known, with the relation (2.6) and (2.7) one can estimate the number of grid nodes and number of time steps required to resolve the flow at the Kolomogorov scales. Because both spatial and temporal resolutions grow exponentially with Re, application of DNS to simulation of engineering problems at high Reynolds numbers (e.g., flow in gas turbines) is usually prohibited due to the high demands for computational resources. However, given the fact that Reynolds number is typically low in blood vessels, DNS becomes a practical and promising numerical tool for simulation of blood flows.

2.4 Numerical Algorithm

A finite volume method is used to discretise the governing equations to yield a system of linear algebraic equations. The diffusion term in the momentum equations is discretised using a second-order accurate central difference scheme and the convective term is discretised using the energy conserving discretisation scheme of Morinishi *et al.* [53]. The transient term was discretised using a three-point backward difference scheme and the time step is $\Delta t = 1.5 \times 10^{-3}$ sec. A Poisson type pressure correction equation is solved using an incomplete Cholesky conjugate gradient (ICCG) [54] method at each time step to update the pressure field. The checkerboard effect in the

pressure field arising from the pressure-velocity decoupling on a collocated grid system was removed using a nonlinear momentum interpolation scheme [55]. A BI-CGSTAB solver was used to solve the matrix of velocity vectors. Overall, the in-house code is second-order accurate with respect to both temporal and spatial resolutions.

The current parallel code was developed using OpenMP based on a serial FORTRAN code (Molla *et al.* [7] and Hossain [56]) revised from the LES-BOFFIN code of Jones *et al.* [48, 49]. The detailed discretization schemes and algorithm of the serial N-S solver for numerical simulation of pulsatile stenotic flows have been well-documented in Hossain [56].

2.5 Boundary Conditions

The physiological pulsatile laminar velocity profile used for generating the time-dependent pulsatile boundary condition at the inlet of the channel, was obtained by analytically solving the Navier-Stokes equation in the context of a fully-developed laminar channel flow when the pressure gradient is approximated as a temporal Fourier series, $\frac{\partial p}{\partial x} = \frac{2}{3}A_0 - A\sum_{n=1}^{N} M_n e^{i(n\omega t+\phi_n)}$ (see, Womersley [57]). The solution takes the following form [56]:

$$u(y,t) = U[1 - 4\frac{y^2}{h^2}] + A\sum_{N}^{n=1} \frac{M_n h^2}{in\mu\alpha^2}[1 - \frac{\cosh(\sqrt{in}\alpha\frac{y}{h})}{\cosh(\sqrt{in}\alpha\frac{1}{2})}]e^{i(n\omega t+\phi_n)} \qquad (2.8)$$

In the above equation, thae constants A_0 and A correspond to the steady and oscillatory parts of the pressure gradient; M_n and ϕ_n represent coefficients and the phase angle, respectively; N is the number of harmonics of the flow set to 4; $\omega \stackrel{\text{def}}{=} \frac{2\pi}{T}$ is the frequency of the pulsations, and T is the time period of a pulsation cycle; i is imaginary unit, $\sqrt{-1}$; and U, μ and h are bulk velocity, viscosity of the fluid and height of the channel, respectively. The real part of this solution (Eq. (2.8)) is used as an inlet boundary condition to generate the pulsatile flow.

At the outlet of the channel, the convective boundary condition is used, viz.

$$\frac{\partial u_i}{\partial t} + U_c \frac{A_{kj}}{|\mathbf{J}|} \frac{\partial u_j}{\partial \xi_k} = 0 \tag{2.9}$$

where U_c is the mean convective velocity at the outlet.

In the spanwise direction, a periodic boundary condition is applied. Thus the field at two spanwise boundaries Γ_1 and Γ_2 is set to be identical, i.e.,

$$u_j(x;t)|_{\Gamma_1} = u_j(x;t)|_{\Gamma_2} \tag{2.10}$$

$$p(x;t)|_{\Gamma_1} = p(x;t)|_{\Gamma_2} \tag{2.11}$$

No slip and no penetration boundary condition is applied to all solid surfaces. This boundary condition is used for both the lower and upper walls of the model, which is defined as

$$u_j(x;t)|_{\Gamma} = 0 \tag{2.12}$$

2.6 Calculation of Flow Statistics

Owing to the presence of pulsations, it requires that the calculation of statistics needs to be carefully dealt with. Three averaging techniques are used in this research, including phase averaging between different pulsation cycles, time-averaging, and spatial-averaging along the homogeneous (spanwise) direction. Furthermore, these three averaging methods need to be properly coupled in the calculations in order to reveal properly the statistical properties of the pulsatile flow field. In general, the statistical method adopted here is similar to those used in Mittal *et al.* [58] and Varghese *et al.* [3]. The basic concepts of these averaging techniques will be now clarified.

For a generic flow variable in DNS, f, time-averaging over the period of time T_f

is defined as

$$\langle f \rangle (x, y, z) = \frac{1}{T_f} \int_{t_0}^{t_0+T_f} f(x, y, z, t) dt \tag{2.13}$$

where t_0 is the initial time and $T_f = NT$ and N is the total number of pulsatile cycles. Following the convention, turbulent fluctuations of the flow variable f with respect to time-averaging can be determined through the following decomposition

$$f^{'}(x, y, z, t) = f(x, y, z, t) - \langle f \rangle (x, y, z) \tag{2.14}$$

In the spanwise direction, the flow field is statistically homogeneous. Spatial-averaging along the spanwise direction can be performed as

$$\langle f \rangle_s (x, y, t) = \frac{1}{L_z} \int_0^{L_z} f(x, y, z, t) dz \tag{2.15}$$

where $L_z = 3h$ is the width of the channel. In order to separate small turbulent fluctuations from the large pulsatile fluctuations, a phase-averaging technique is needed (Hussain and Reynolds [59] and Mittal *et al.* [58]). Phase-averaging over T_f (for N pulsatile cycles) is defined as

$$\langle f \rangle_p (x, y, t) = \frac{1}{N} \sum_{n=0}^{N-1} \langle f \rangle_s (x, y, t + nT) \tag{2.16}$$

In order to determine the root mean square (RMS) of a flow variable, all three averaging techniques mentioned here are needed. First, both phase-averaging and spatial-averaging (spanwise) are applied to all pulsatile cycles; and second, an instantaneous field (of the same phase) is compared with the phase- and spatial-averaged field to extract the random fluctuations within each pulsatile cycle. After completing these two steps, the influence of large pulsation fluctuations (see, Fig. 4.2(a)) on the obtained random fluctuating field is removed, which can be thereafter considered as statistically homogeneous with respect to time at an arbitrary

spatial location. The random fluctuating field is calculated as

$$f''(x,y,z,t) = f(x,y,z,t) - \langle f \rangle_{sp}(x,y,t) \tag{2.17}$$

Based on the above steps, it is now possible to use time-averaging to determine the RMS values over the total computational time T_f

$$f_{rms} = \sqrt{\frac{1}{T_f}\int_{t_0}^{t_0+T_f} f''^2 dt} \tag{2.18}$$

In the above equations, subscripts p and s are used to denote phase-averaging and spatial-averaging, respectively.

In the next section, a pair of angular brackets $\langle . \rangle$ will be used to represent a time-averaged quantity following Eq. (2.13) during the analysis of numerical results. However, without causing any confusion in symbolism, if a homogeneous dimension presents (typically, along the spanwise direction of the domain), this angular bracket operator will also imply an additional spatial averaging with respect to that particular homogeneous dimension [56].

Chapter 3

Parallel Programming with OpenMP

3.1 Introduction

Open Multiprocessing (OpenMP) is a shared-memory application programming interface (API) which allows the facility to use shared-memory parallel (SMP) programming. The advantage of parallel computers over classical supercomputers is scalability. In general, a parallel computing strategy can reduce the execution time of a program significantly in comparison with a sequential computing strategy. To facilitate parallel computing, available parallel computers may consist of thousands of processors and terabytes of memory.

OpenMP was developed to enable portable shared-memory parallel programming. It aims to support parallelization of scientific and engineering computations from many disciplines including CFD applications. Moreover, it is intended to provide an approach that is relatively easy to learn as well as to implement. The API is designed to permit an incremental approach to parallelizing an existing serial code, in which portions of a program can be parallelized. In OpenMP, a single set of source files contains the code for both the serial and the parallel versions of a program which makes it simple and convenient to use.

3.2 Parallel Programming

Parallel programming is designed as a symmetric multiprocessor system. Individual processors of a shared-memory parallel computer share memory in such a way that each of them can access any memory location with the same speed. Many small shared-memory machines are symmetric in this sense. There are different ways to parallelize computer programming codes by using shared-memory machines based on OpenMP, message passing interface (MPI), etc.

3.2.1 OpenMP

OpenMP is suitable for implementation on a broad range of applications. It is not a new programming language; rather, it is notation that can be added to a sequential program in FORTRAN, C, or C++. These notations describe how the work is to be shared among threads that will execute on different processors and to order access to shared data as needed. The appropriate insertion of OpenMP notations into a sequential program allows many applications to benefit from shared-memory parallel architectures often with minimal modifications to the code.

There are some factors involved in successful use of OpenMP. Primarily, it is highly focused on structured parallel programming. It is also comparatively simple to use as the burden of working out the details of the parallel program is automatically taken care of by the compiler. As OpenMP is widely accepted as a parallel programming strategy, an OpenMP application will run on many different platforms. In summary, OpenMP is a standard shared-memory programming strategy which is easy to learn and apply, and has been accepted positively in the research community.

3.3 General Description of OpenMP

OpenMP builds on a large body of work that supports the specification of programs for execution through a collection of cooperating threads [60]. If multiple threads collaborate to execute a program, they need to share the resources, including the address space of the corresponding process. The individual threads need a program counter and a space in memory to save variables that are specific to it. Threads running simultaneously on multiple processors or cores may work concurrently to execute a parallel program. Multi-threaded programs can be written in various ways, some of which permit complex interactions between threads.

OpenMP attempts to provide ease of programming and to help the user avoid a number of potential programming errors by offering a structured approach to multi-threaded programming. It supports the so-called fork-join programming model [61]. Under this approach, the program starts as a single thread of execution, just like a sequential program. The thread that executes this code is referred to as the initial thread. Whenever an OpenMP parallel construct is encountered by a thread while it is executing the program, it creates a team of threads, i.e., the "fork", becomes the master of the team, and collaborates with the other members of the team to execute the code enclosed by the construct. At the end of the construct, only the original thread, or master of the team, continues, whereas all others terminate, i.e., the "join". Each portion of code enclosed by a parallel construct is called a parallel region.

OpenMP expects the application developer to give a high-level specification of the parallelism in the program and the method for exploiting that parallelism. Thus it provides notations for indicating the regions of an OpenMP program that should be executed in parallel. It also allows for the provision of additional information on how this is to be accomplished. The job of the OpenMP implementation is to sort out the low-level details of actually creating independent threads to execute the code and to assign work to them according to the strategy specified by the programmer.

3.4 Specialty of OpenMP

OpenMP comprises a set of compiler directives, runtime library routines, and environment variables to specify shared-memory parallelism in FORTRAN and C/C++ programs. An OpenMP directive is a specially formatted comment that generally applies to the executable code immediately following it in the program. An OpenMP directive generally affects only those threads that encounter it. Many of the directives are applied to a structured segment of code. Each structured segment has a sequence of executable statements with a single entry at the top and a single exit at the bottom in FORTRAN programs, and an executable statement in C/C++. In FORTRAN programs, the start and end of a segment of code are explicitly marked by OpenMP directives.

OpenMP provides means for a programmer to create teams of threads for parallel execution and specify how to share work among the members of a team. The programmer can declare both shared and private variables explicitly. Finally, OpenMP compilers synchronize threads and enable them to perform certain operations exclusively.

3.5 Programming with OpenMP

OpenMP directives have the flexibility to give the instructions to the compiler to execute the code in parallel. They also instruct the compiler how to assign the work among the threads that will run the code. An OpenMP directive is an instruction format that is understood by OpenMP compilers only. It looks like a comment to a regular FORTRAN compiler, such that if a compiler is not OpenMP-aware, the program will be identified as sequential.

To create an OpenMP program from a sequential one, it is necessary to identify the parallelism it contains. The most important things in identifying parallelism are finding instructions, sequences of instructions, and even large regions of code that

may be executed simultaneously by different processors. The developer must identify portions of a code to obtain independent instruction sequences. Sometimes it may be necessary to replace an algorithm with an alternative one that accomplishes the same task. This can be a challenging problem which needs a good deal of knowledge about the algorithms. There are some typical kinds of parallelisms in programs, and a variety of strategies are available to make them ready for parallel executions.

After identifying the parallelism in a sequential program, it is necessary to express the parallelism by using OpenMP directives. The major advantage of OpenMP is that it can be applied incrementally to create a parallel program from an existing sequential code. The developer can insert directives into a portion of the code, then compile and test the code, followed by another portion of the code to be parallelized. The programmer can finish the parallelization of sequential code once the desired speedup has been obtained.

3.6 OpenMP Performance

In terms of performance evaluation, it is important to signify the reduction of code execution time after OpenMP parallelization of a sequential program. If T_1 denotes the execution time of an application on 1 processor, then in an ideal situation, the execution time on P processors should be T_1/P. Let T_P denote the execution time on P processors, and then the parallel speedup, S can be defined as

$$S = \frac{T_1}{T_P} \tag{3.1}$$

By using an increasing number of processors, the execution time is reduced in the parallelized parts of the program. Eventually the execution time is dependent upon the time taken to compute the sequential portion. This effect, known as Amdahls law, can be formulated as

$$S = \frac{1}{f_{par}/P + (1 - f_{par})} \tag{3.2}$$

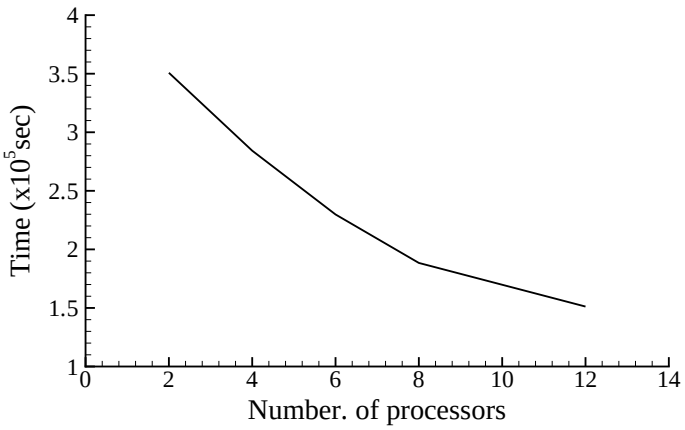

FIGURE 3.1: Parallel performance based on code execution time with the number of processors.

where f_{par} is the parallel fraction of the code and P is the number of processors. In the ideal case when the entire code runs in parallel, $f_{par} = 1$, the expected speedup is equal to the number of processors. If only 90% of the code runs in parallel ($f_{par} = 0.9$), the maximal speedup one can expect on 8 processors is 4.7 and on 16 processors is 6.4. So it is important to parallelize as much of the code as possible especially when large numbers of processors are in use.

A measure of a program's ability to decrease the execution time of the code with an increasing number of processors is referred to as parallel scalability. To understand the effect of using a multiprocessor system, a test has been conducted. In Fig. 3.1, the time required for code executed in parallel is plotted against the number of processors. It is clearly seen that the execution time has reduced significantly with the increasing number of processors. But the reduction in the execution time is not linear because some part of the code cannot be parallelized using OpenMP.

Chapter 4

DNS of a Physiological Pulsatile Newtonian Flow in a Model Arterial Stenosis

4.1 Introduction

In this chapter, DNS is used to simulate the physiological pulsatile flow in a constricted channel to gain insights into the transition-to-turbulent flow in an artificial arterial stenosis. The Womersley number tested was fixed to 10.5 and the Reynolds number was varied from 500 to 2000 in the simulation. In order to understand the effects of constriction on the flow field in a channel, degree of stenosis were varied from 50% to 75%. The physical characteristics of the flow field have been analyzed in terms of the mean streamwise velocity, RMS velocities, TKE, viscous wall shear stress and wall pressure.

4.2 Test Case

The computational domain consists of a 3D channel with a symmetric cosine-shaped stenosis on the upper and lower walls (shown previously in Fig. 1.1). Due to the presence of the stenosis, the height of the channel, δ, is a variable in the streamwise direction, i.e., $\delta = \delta(x)$. Away from the stenosis, the height of the channel is

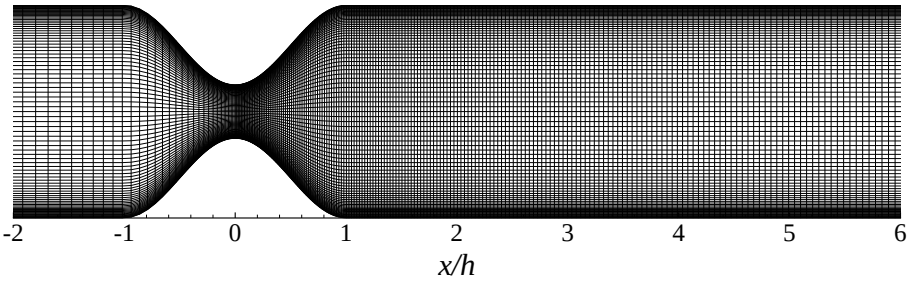

FIGURE 4.1: Schematic of mesh configuration in x-y plane with 75% degree of stenosis.

constant and is represented here using h, i.e., $\delta = h$ in the region either upstream or downstream of the stenosis. The width of the channel is set to $3h$. Both stenoses are centered at $x/h = 0$. In Fig. 1.1, x, y and z are used to represent the streamwise, vertical and spanwise coordinates, respectively. The stenosis is $5h$ downstream of the channel inlet and $15h$ away from the channel outlet. The form of the stenosis chosen for this study is

$$\frac{y}{h} = 1 - \frac{f_c}{2}\left(1 + \cos\frac{x\pi}{h}\right), \quad -h \leq x \leq h \tag{4.1}$$

where $f_c = \delta_{min}/h$ is a parameter for controlling the height of the stenosis. In the present study, f_c is set to $\frac{1}{2}$, $\frac{3}{5}$ and $\frac{3}{4}$, which results in 50%, 60% and 75% reduction of the cross-sectional area at the centre of the stenosis, respectively.

Figure 4.1 shows the schematic of the mesh configuration in the x-y plane. As the no-slip condition is applied on the top and bottom walls of the channel, the meshes are refined near the top and bottom walls to increase the resolution in the near-wall regions. The mesh lines are also concentrated at the centre and immediate downstream of the stenosis because these are the regions where energetic eddies are generated and boundary-layer separation occurs. The mesh is uniform in the spanwise direction. As discussed in the chapter 2, the requirement on the order of magnitude of spatial and temporal resolutions in a DNS is estimated based on the Reynolds number. The numerical results for $Re = 1200$ presented in this chapter are based on the grid system with $350 \times 90 \times 90$ control volumes (in the streamwise, vertical and spanwise directions, respectively). As the grid system with $350 \times 90 \times 90$ was able to resolve the smallest scale of turbulence at $Re = 1200$, it is fine enough to resolve the

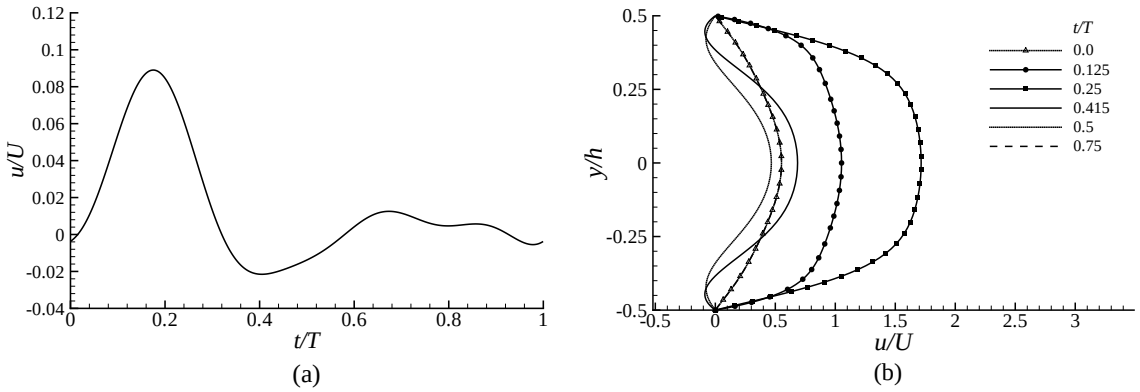

FIGURE 4.2: Instantaneous inlet velocity u/U for $\alpha = 10.5$: (a) time history near the wall ($x/h = -5.0, y/h = 0.01, z/h = 1.5$), and (b) at the different time phases for $Re = 1200$.

smallest Kolmogorov's scales at $Re = 500$.

4.3 Inflow Boundary Condition

In the simulations, the Womersley number is defined as $\alpha^2 \stackrel{\text{def}}{=} h^2 \frac{\rho\omega}{\mu}$, where ρ is the density of the fluid and α is the Womersley number which reflects the ratio of the pulsatile inertial forces to the viscous forces. If the Womersley number is small (for $\alpha \leq 1$), the frequency of pulsations is low and the viscous forces dominate flow; and consequently, a cross-sectional parabolic velocity profile develops in response to the instantaneous streamwise pressure gradient (i.e., the Poiseuille flow behavior) during each pulsation cycle. However, according to Ku [2], if the Womersley number is large (for $\alpha \geq 10$), the frequency of pulsations is high and the pulsatile inertial forces play an important role; and consequently, the phase of the velocity field development lags behind the phase of the instantaneous streamwise pressure gradient (which implies that the flow behavior deviates from the Poiseuille type). In the present simulation, the Womersley number is fixed to $\alpha = 10.5$.

In Eq. 2.8, the value of the amplitude of oscillation, A, varies with the Reynolds number to maintain the maximum flow rate at the inlet. For $Re = 500$, 1200, and 2000, the value of A is set to 0.1, 0.25 and 0.4, respectively. For the four different harmonics, the value of M_n is 0.78, 1.32, -0.74 and -0.41 and the value of ϕ_n

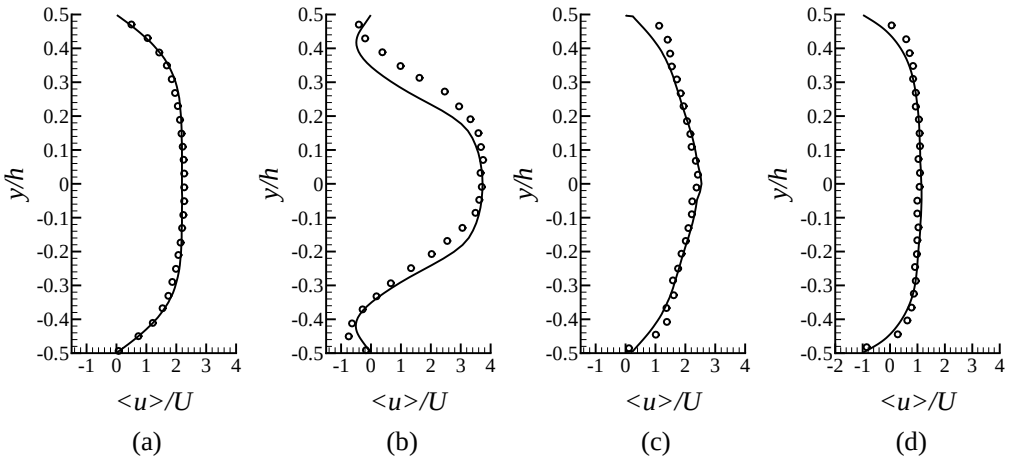

FIGURE 4.3: Comparison of phase-averaged $\langle u \rangle / U$ with the experimental results of Beratlis *et al.* [1], at (a) $x/h = -10$, (b) $x/h = 2$, (c) $x/h = 4$, and (d) $x/h = 6$. Circular symbol for experiment, solid line for present DNS.

is 0.0113446, −1.4442599, 0.4625122 and −0.2879793, respectively [57]. The inlet pulsatile velocity profile, derived from Eq. (2.8), is demonstrated in Fig. 4.2. The time history of the velocity field during a full pulsatile cycle at a specific near-wall location in the crossing line of the spanwise vertical inlet plane ($x/h = -5$) and the central streamwise vertical plane ($z/h = 1.5$) of the domain is shown in Fig. 4.2(a). The temporal variation of the vertical velocity profile across the centre of the inlet plane at different phases over a pulsatile cycle is shown in Fig. 4.2(b).

4.4 Results and Analysis

In order to examine the predictive accuracy of our numerical algorithm, the in-house code has been validated using a bench test case. The numerical results obtained have been compared with the experimental data (on a post-stenotic flow) of Beratlis *et al.* [1]. Beratlis *et al.* [1] conducted the experiment to investigate pulsatile flow in a stenotic channel using a single-component LDV. Their measurement system consisted of a Dantec instrument and computer controlled traverse system. In order to be consistent with their experimental conditions, the mean bulk velocity was set to $U = 0.082$ m/s, with an oscillatory amplitude of $\Delta U = 0.06$ m/s and a period of $T = 4$

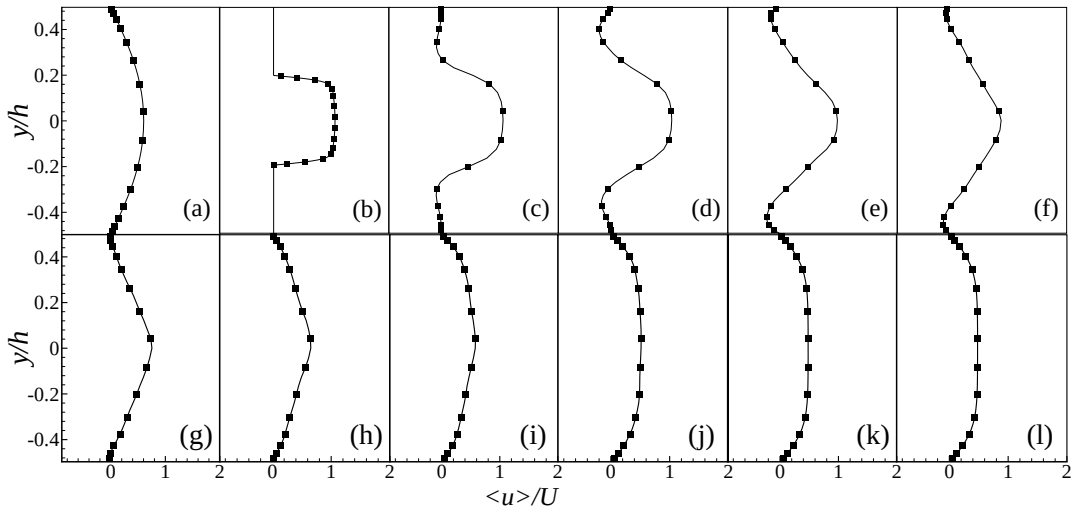

FIGURE 4.4: Grid sensitivity test with respect to the mean streamwise velocity $\langle u \rangle / U$ at (a) $x/h = -5.0$ (inlet), (b) $x/h = 0.0$, (c) $x/h = 1.0$, (d) $x/h = 2.0$, (e) $x/h = 3.0$, (f) $x/h = 3.5$, (g) $x/h = 4.0$, (h) $x/h = 4.5$, (i) $x/h = 5.0$, (j) $x/h = 6.0$, (k) $x/h = 10.0$, and (l) $x/h = 15.0$ (outlet). Based on two grid systems, Case 1: solid line for $350 \times 90 \times 90$ control volumes, Case 2: solid line with symbol for $350 \times 120 \times 90$ control volumes.

sec. The corresponding Reynolds and Womersley numbers were set to $Re = 570$ and $\alpha = 8.25$, respectively, and at the inlet, the pulsatile boundary condition described in the previous subsection was used. Figure 4.3 shows the phase-averaged streamwise velocity at different downstream locations, and it is evident that the present DNS has well reproduced experimental results of Beratlis *et al.* [1]. At the stenosis, the maximum streamwise velocity is seen in Fig. 4.3(b) and the flow begins to accelerate. In the immediate post-stenotic region, two recirculation zones are generated which shows that the mean velocity is negative. In addition, the thin shear layer becomes unstable and rolls up into vortices, which subsequently interact with the recirculating areas and the flow becomes re-laminarized in the far downstream region.

In order to thoroughly examine the effects of grid resolution on the predicted results, two different grid systems with $350 \times 90 \times 90$ (Case 1) and $350 \times 120 \times 90$ (Case 2) control volumes (in the x, y and z directions, respectively) were compared at $Re = 1200$. The two grid systems are body-fitted reflecting the curvilinear geometry of the computational domain. The number of streamwise grid points upstream of the stenosis is always fixed to 50 while the rest of the grid points are distributed

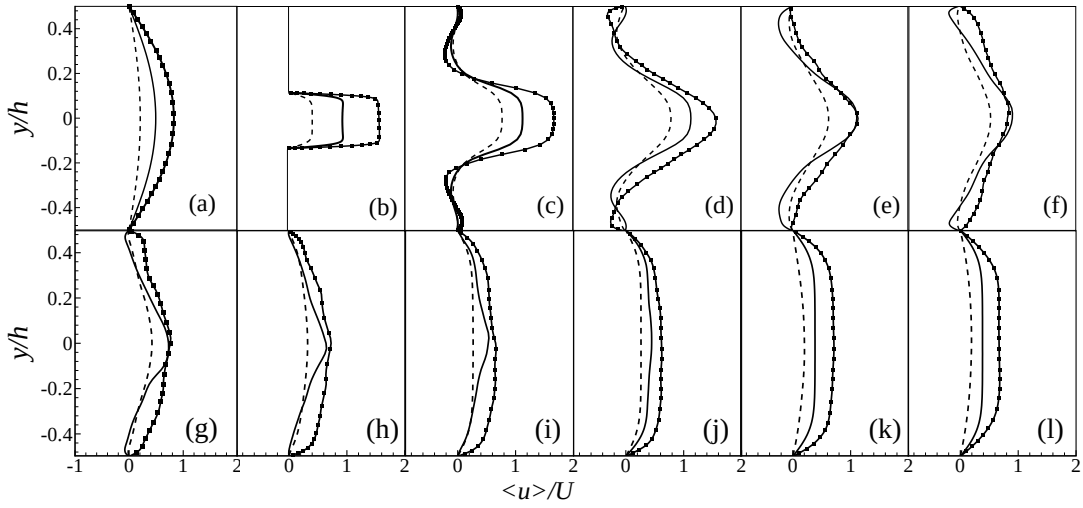

FIGURE 4.5: The mean streamwise velocity $\langle u \rangle / U$ at (a) $x/h = -5.0$ (inlet), (b) $x/h = 0.0$, (c) $x/h = 1.0$, (d) $x/h = 2.0$, (e) $x/h = 3.0$, (f) $x/h = 3.5$, (g) $x/h = 4.0$, (h) $x/h = 4.5$, (i) $x/h = 5.0$, (j) $x/h = 6.0$, (k) $x/h = 10.0$, and (l) $x/h = 15.0$ (outlet). Based on three Reynolds numbers, Case 1: dashed line for $Re = 500$, Case 2: solid line for $Re = 1500$, and Case 3: solid line with symbols for $Re = 2000$.

within and downstream of the stenosis. The grid is uniform in the spanwise direction and significantly refined in the near-wall region in order to accurately resolve the wall shear stress. The results of Cases 1 and 2 are compared in Fig. 4.4 in terms of the non-dimensionalized time-averaged streamwise velocity (i.e., $\langle u \rangle / U$) at different locations along the streamwise direction. From Fig. 4.4, it is seen that two grid configurations used in the present computations can predict correctly the mean velocity field and are not sensitive to the grid resolution.

4.4.1 Flow Characteristics

Figure 4.5 shows the mean streamwise velocity $\langle u \rangle$ (non-dimensionalized using the bulk velocity, U) at different streamwise locations for $Re = 500$, 1200, and 2000. As shown in Fig. 4.5(b), at the centre of the stenosis ($x/h = 0$), the flow velocity reaches its maximum value. Triggered by the stenosis, the flow field driven by the pulsatile inlet condition undergoes laminar-turbulent-laminar patterns in the streamwise direction (see also Figs. 4.6- 4.8). The flow becomes turbulent immediately

after the throat location ($x/h = 0$) of the stenosis. In the far downstream region ($x/h \geq 6$), the flow becomes re-laminarized, and the velocity profile re-establishes itself to a shape similar to that at the inlet. From Fig. 4.5, it can also be seen that mean streamwise velocity increases with the Reynolds number at different streamwise locations to reflect the principle of mass conservation.

The presence of the stenosis not only accelerates the flow (see Fig. 4.5(b)) but also causes boundary layer separation at the top and bottom walls immediately after the stenosis. The separation of the boundary layers further results in recirculation of the flow. As evident in Figs. 4.5(c)-(g), the mean velocity is negative close to the top and bottom walls, which is an indication of recirculation flow pattern (in the post-stenotic region). By comparing the velocity profiles of the three Reynolds numbers, it is interesting to observe that the size of the recirculation bubble (in terms of height and length) varies with the Reynolds number. A more careful analysis of the Reynolds number effects on the recirculation of the flow will be conducted later using Figs. 4.8 and 4.9 based on the contours of the instantaneous streamwise velocity.

Figures 4.6 and 4.7 show the slice view of the isopleths of the non-dimensionalized instantaneous streamwise velocity field u/U at $t/T = 10.25$. In Fig. 4.6, the first two slices show that prior to the stenosis, the flow is laminar and stratified. The third slice shows that the velocity reaches its maximum at the throat location ($x/h = 0$) of the stenosis. The fourth slice shows a very interesting instantaneous flow pattern: in the immediate post-stenotic region, the velocity is very large (as indicated by the red color) at the centre of the channel, however, the velocity is negative in the recirculation region close to the upper and lower walls. This pattern is consistent with the previous observation of the mean velocity profiles in Fig. 4.5. Turbulence is triggered by the stenosis. However, as indicated by the last four slices, gradually, the flow becomes re-laminarized in the far downstream region. The flow physics discussed here are also clearly demonstrated in Fig. 4.7, which shows the contours of the instantaneous streamwise velocity profiles in the central x-z plane at two Reynolds numbers 500 and 1200. From both Figs. 4.6 and 4.7, it is observed that due to the presence of the stenosis, the flow is triggered to a weakly turbulent state at $Re = 500$ but to a fully

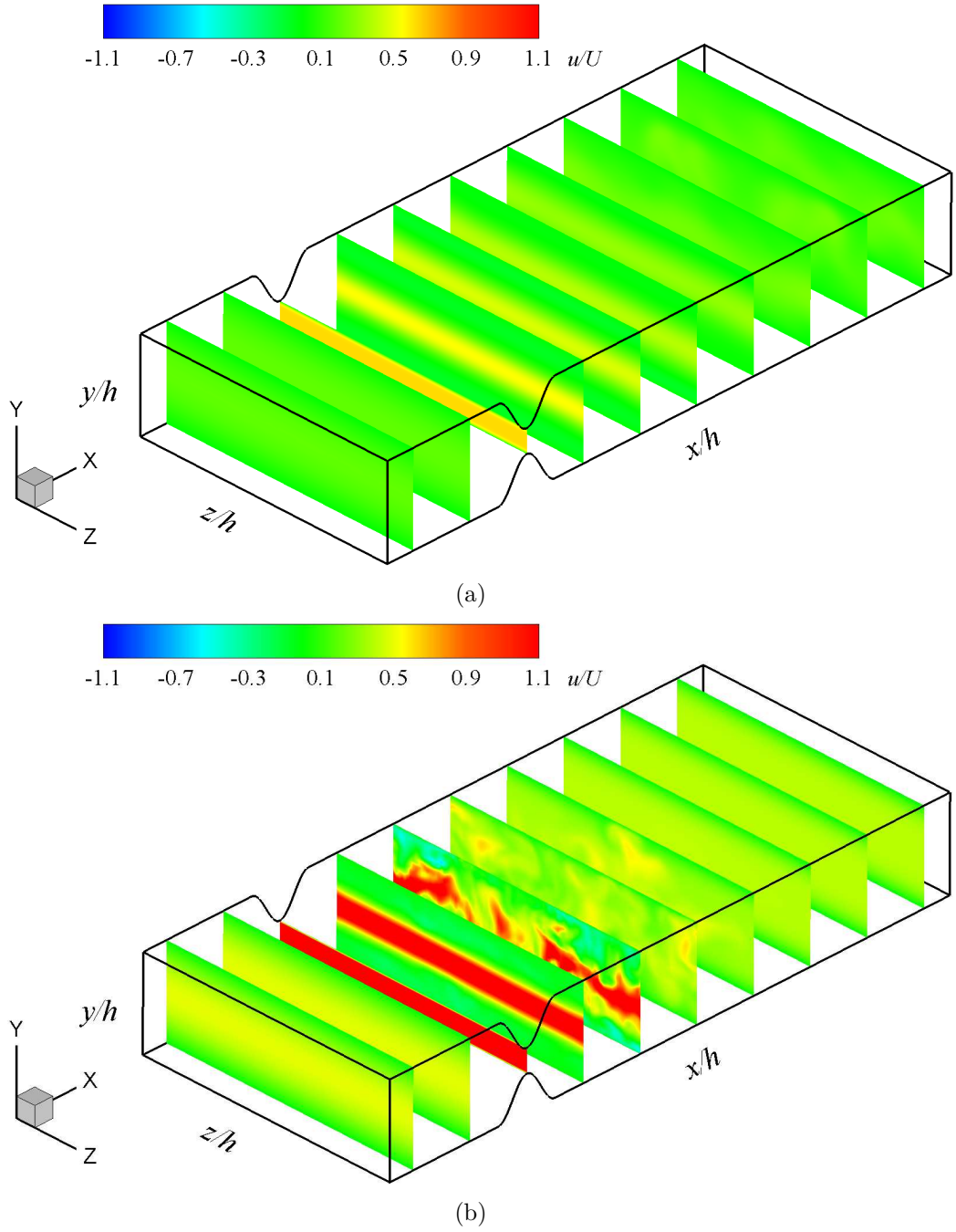

FIGURE 4.6: Slice view of instantaneous streamwise velocity u/U at $t/T = 10.25$ for (a) $Re = 500$, and (b) $Re = 1200$.

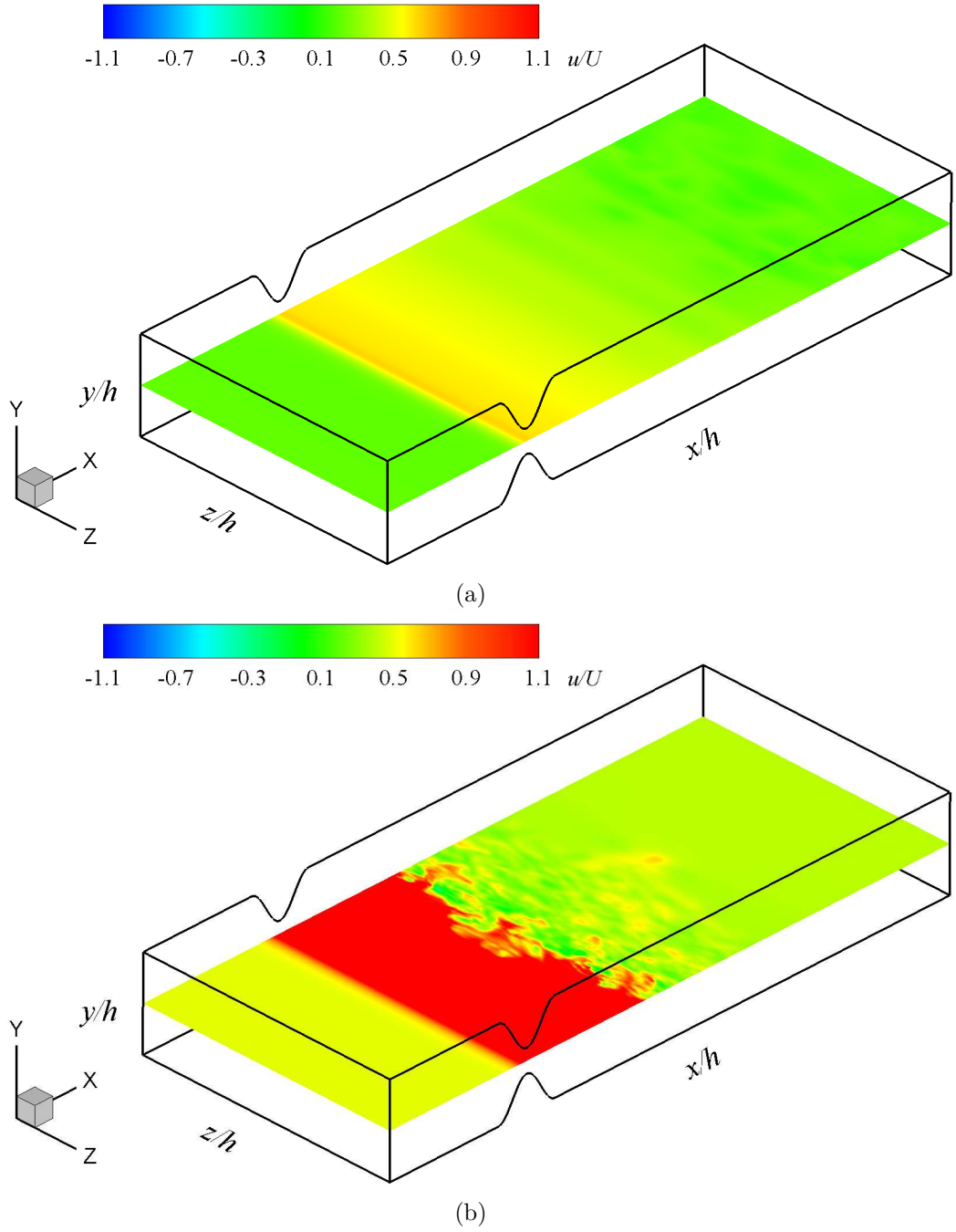

FIGURE 4.7: Contours of instantaneous streamwise velocity u/U in the central x-z plane with degree of stenosis 75% at $t/T = 10.25$ for (a) $Re = 500$, and (b) $Re = 1200$.

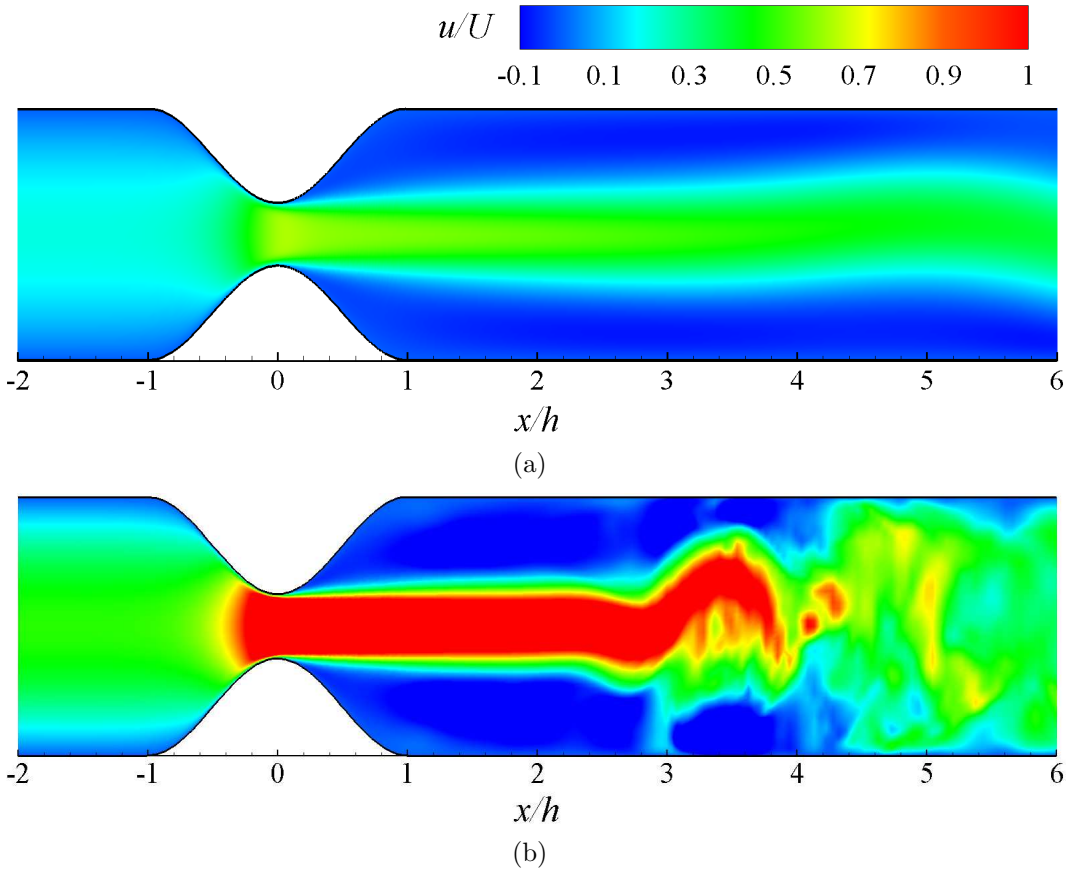

FIGURE 4.8: Contours of the instantaneous streamwise velocity u/U in the central x-y plane at $t/T = 10.25$ for (a) $Re = 500$, and (b) $Re = 1200$.

turbulent state at $Re = 1200$ immediately downstream of the stenosis.

Figures 4.8(a), 4.8(b) and 4.9 illustrate the contours of the instantaneous streamwise velocity at the central plane ($z/h = 1.5$) for $Re = 500$, 1200, and 2000, respectively. The instantaneous vortical structures of the flow are visualized using the contours of instantaneous streamwise velocity, u/U. For three Reynolds numbers tested, two distinct recirculation regions appear near the post-lip of the stenosis due to the separation of the shear layer induced by the stenosis. By comparing Figs. 4.8 (a) and (b), it is observed that the flow reattaches earlier at the higher Reynolds number, which agrees qualitatively with the result of Ahmed and Giddens [11, 12] and Mittal *et al.* [58]. At $Re = 500$ and 1200, the location of separation is $(x/h)_{sep} = 0.203$ and 0.157 and the location of reattachment is $(x/h)_{reatt} = 8.92$ and 4.17, respectively. At $Re = 2000$, another interesting comparison is made at varying degree of stenosis of

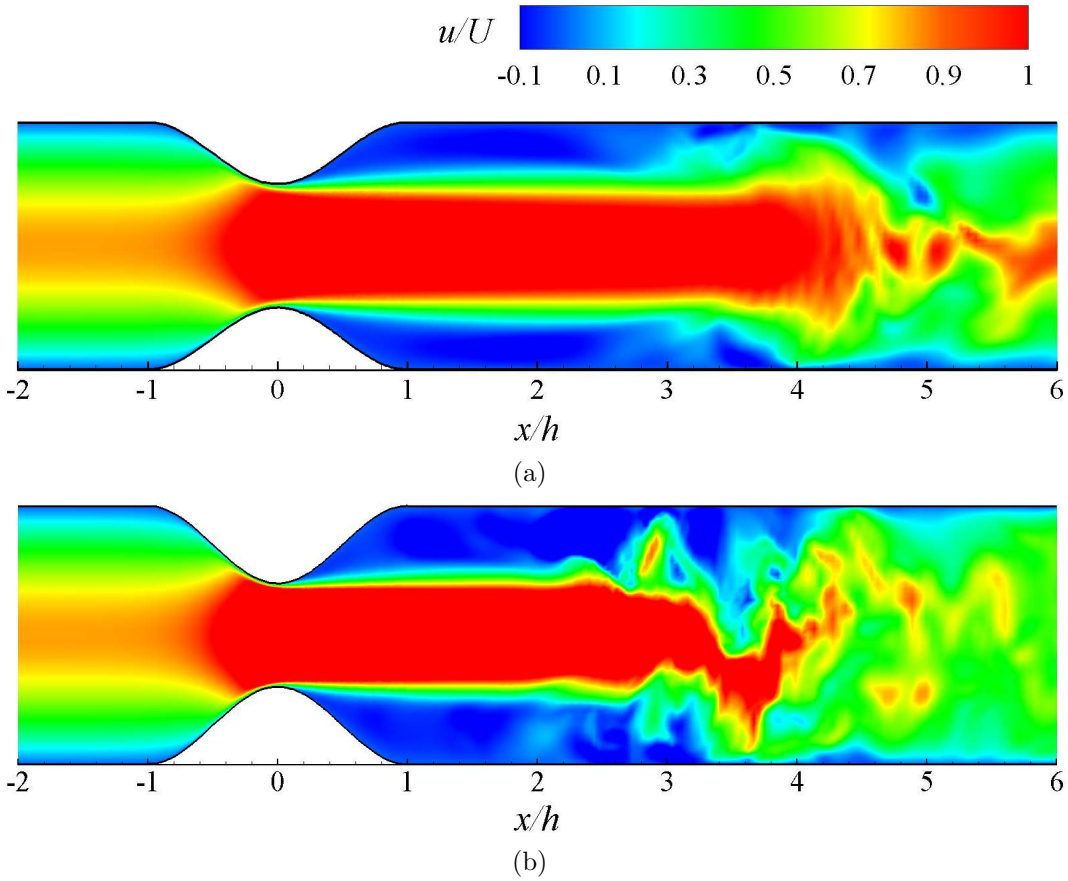

FIGURE 4.9: Contours of the instantaneous streamwise velocity u/U in the central x-y plane for $Re = 2000$ at $t/T = 10.25$ with degree of stenosis of (a) 50%, and (b) 60%.

50% and 60%, for which, the location of separation is $(x/h)_{sep} = 0.235$ and 0.188 and the location of reattachment is $(x/h)_{reatt} = 3.94$ and 3.44, respectively. Therefore, it is seen that the flow reattaches earlier at the higher degree of stenosis. As the degree of stenosis increases, the flow velocity increases as a result of a narrower cross-sectional area at the throat location of the stenosis. Therefore, the local Reynolds number also increases for the higher degree stenosis case. The above observation is in analogy with the dynamics of a confined jet, in which the flow also reattaches earlier as the Reynolds number increases.

In Fig. 4.10, the cycle-to-cycle flow development is shown using the contour plots of the streamwise velocity u (non-dimensionalized using the bulk velocity, U). In Fig. 4.10(a), it is observed that at the end of the first cycle, two small recirculation

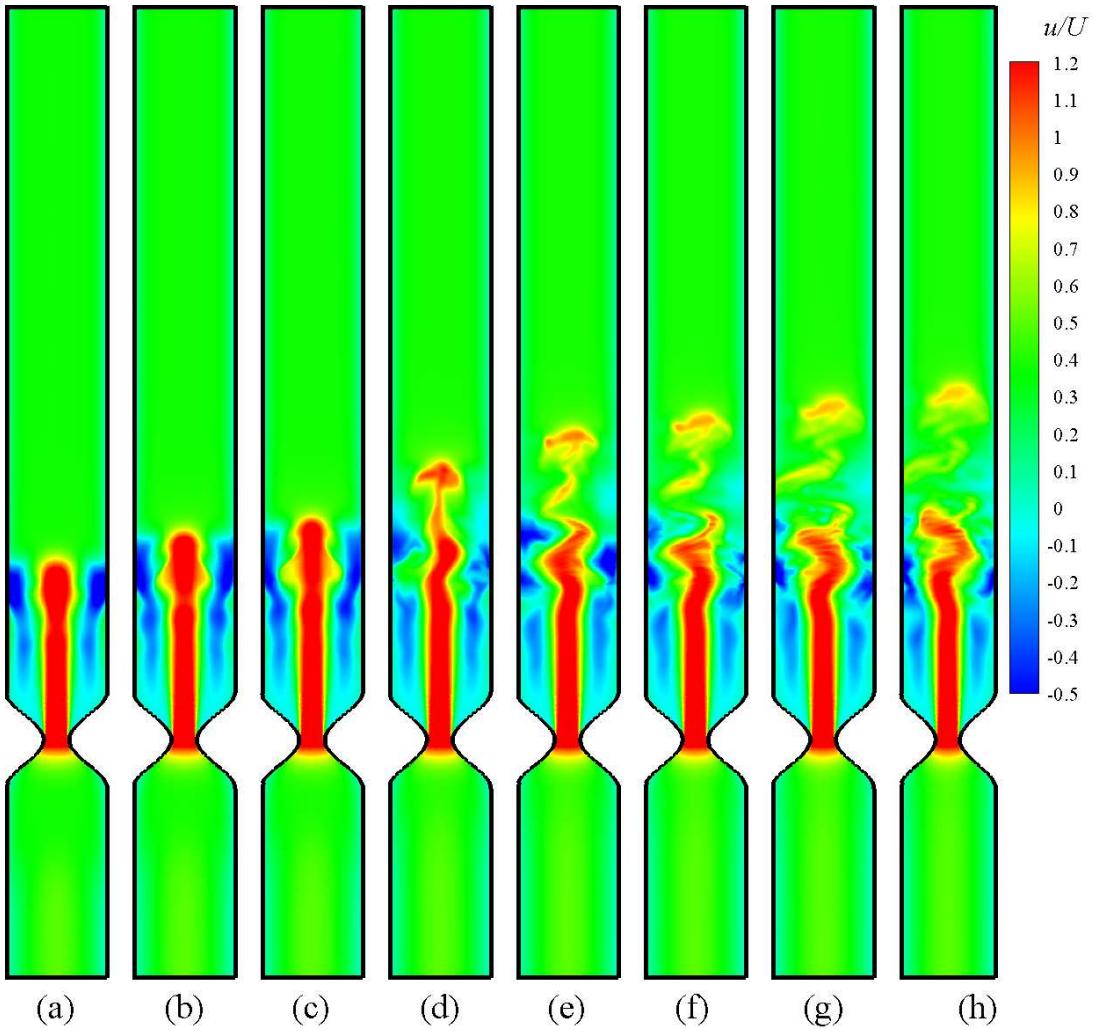

FIGURE 4.10: Contours of the instantaneous streamwise velocity u in the central x-y plane at (a) $t/T = 1.25$, (b) $t/T = 2.25$, (c) $t/T = 4.25$, (d) $t/T = 6.25$, (e) $t/T = 7.25$, (f) $t/T = 8.25$, (g) $t/T = 9.25$, and (h) $t/T = 10.25$ for $Re = 1200$.

regions near the two walls are created. A primary shear layer which is initially generated at the centre of the stenosis propagates towards the downstream region at the end of the second cycle (see Fig. 4.10(b)). As shown clearly in Figs. 4.10(c)-(h), as the flow field evolves with time, the shear layers elongate and finally break down into vortices and triggers the turbulent flow pattern. The simulation has been carried out up to the end of the tenth cycle, as it has been tested that the solutions eventually reach to a statistically stationary state after the eighth cycle, and the flow statistics accumulated after the eighth cycle, do not vary significantly between the eighth and tenth cycles.

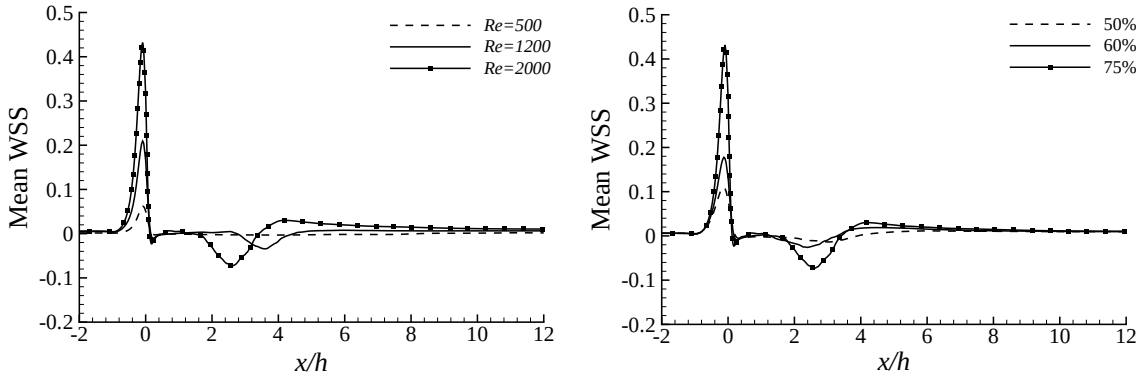

(a) (b)

FIGURE 4.11: Non-dimensionalized time- and spanwise-averaged profiles of the wall shear stress $\langle \tau_w \rangle / \frac{1}{2}\rho U^2$ for (a) different Reynolds numbers and (b) different degrees of stenoses at $Re = 2000$.

4.4.2 Wall Shear Stresses

Figure 4.11(a) displays the profile of the averaged wall shear stress $\tau_w = \mu \frac{\partial u}{\partial y}|_w$ (non-dimensionalized using $\frac{1}{2}\rho U^2$) over the upper and lower walls. The maximum wall shear stress occurs at the throat location ($x/h = 0$) of the stenosis due to the large vertical gradient of the mean streamwise velocity. As shown in Fig. 4.11(a), following a sharp rise close to the centre of the stenosis, the wall shear stress drops rapidly, becomes negative in the region $0 < x/h < 4$, and then slightly rises to an approximately constant small finite value in the further downstream region. The negative value of the wall shear stress is a consequence of the boundary-layer separation and flow recirculation immediately after the stenosis.

In Fig. 4.11(a), a comparison is further made between the three Reynolds numbers tested. It is observed that in general, the predicted wall shear stress increases as the Reynolds number increases. This is because the mean streamwise velocity increases with the Reynolds number (see Fig. 4.5). In Fig. 4.11(b), another comparison is made among the three different degrees of stenosis at $Re = 2000$. As the reduction of the cross-sectional area increases from 50% to 75%, the mean wall shear stress increases. This is because the mean wall shear stress is determined by the mean velocity field, which increases as the channel becomes narrower.

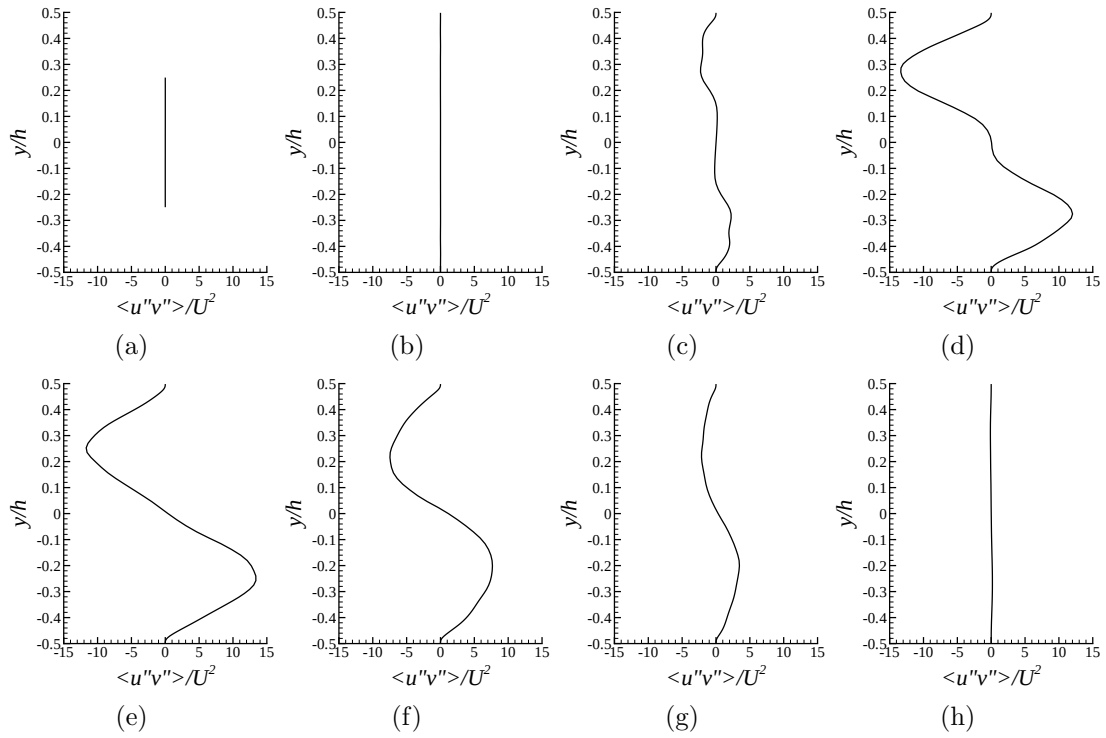

FIGURE 4.12: Non-dimensionalized turbulent shear stress $\langle u''v'' \rangle / U^2$ at (a) $x/h = 0.0$, (b) $x/h = 1.0$, (c) $x/h = 2.0$, (d) $x/h = 3.0$, (e) $x/h = 4.0$, (f) $x/h = 5.0$, (g) $x/h = 6.0$, and (h) $x/h = 10.0$.

The non-dimensionalized turbulent shear stress $\langle u''v'' \rangle / U^2$ is shown in Fig. 4.12 at different streamwise locations. At the throat location ($x/h = 0$) of the stenosis, turbulent shear stress is zero. Turbulence is triggered by the stenosis. As shown in Fig. 4.12, the profiles of the turbulent shear stress is symmetrical in the wall-normal direction, and because of this symmetrical condition, its value is zero in the centre (y/h=0). In the post-stenotic region, turbulent shear stress reduces to zero at the walls due to the no-slip boundary condition. Away from the walls, the turbulent shear stress increases to a peak value from both sides of the walls. As shown in Fig. 4.12(d), the magnitude of the peak value reaches the maximum approximately at $x/h = 3.0$. Following this rise in the turbulent shear stress, the turbulent shear stress drops rapidly, in the region further downstream of the stenosis, and eventually becomes trivial for $x/h \geq 10.0$.

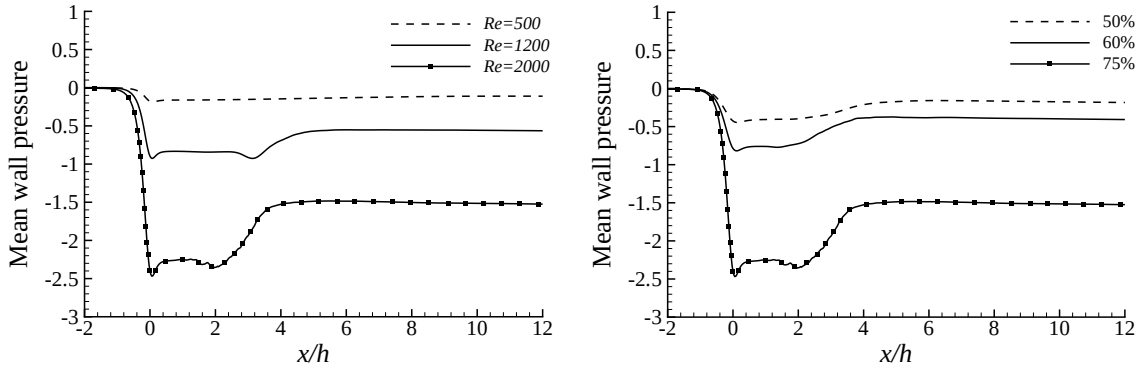

(a) (b)

FIGURE 4.13: Non-dimensionalized time- and spanwise-averaged profile of the wall pressure $\langle p \rangle / \rho U^2$ for (a) different Reynolds numbers at 75% stenosis and (b) different degree of stenoses at $Re = 1200$.

4.4.3 Wall Pressure

The time- and spanwise-averaged wall pressure is shown in Fig. 4.13(a) for the three different Reynolds numbers tested. Owing to the constriction of the channel, the wall pressure drops significantly at the centre of the stenosis. As shown in Figs. 4.13(a) and 4.13(b), the maximum pressure drop occurs within the immediate post-stenotic region for $0 < x/h < 4$, where an adverse pressure gradient presents and flow recirculates. The signature of the flow recirculation pattern is also evident in Figs. 4.5(c)-(g), which show that the mean velocity is negative in the region immediately after the stenosis. Figure 4.13(b) shows the influence of the stenosis contraction percentage on the wall pressure. From Figs. 4.13(a) and 4.13(b), it is evident that the maximum wall pressure drop occurs right at the throat location of the stenosis (for different Reynolds numbers and degrees of stenosis), where the flow speed is the highest. It is evident in Fig. 4.13(b), as the channel becomes narrower (the degree of stenosis increases from 50% to 75%), the wall pressure drops significantly. This is because as the degree of stenosis increases, the flow speeds up which results in a pressure drop. This effect is similar to the increase of the Reynolds number, which results have been shown in Fig. 4.13(a).

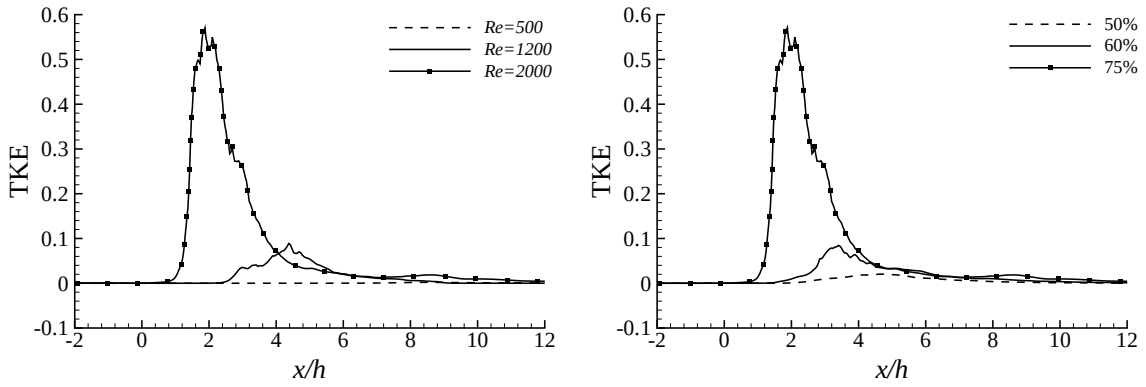

(a) (b)

FIGURE 4.14: Non-dimensionalized time- and spanwise-averaged profile of TKE k/U^2 for (a) different Reynolds numbers at 75% stenosis and (b) different degree of stenoses at $Re = 1200$.

4.4.4 Turbulence Kinetic Energy

Figure 4.14(a) shows the non-dimensionalized time- and spanwise-averaged TKE $k = \frac{1}{2}\langle u_i'' u_i'' \rangle$ of the flow along the streamwise direction for the three different Reynolds numbers tested. Initially, the flow is fully laminar as it is evident that $k = 0$ holds upstream of the stenosis. As soon as the flow passes the centre of the stenosis, turbulence is triggered and the TKE starts to increase rapidly and reaches its maximum value in the immediate post-stenotic region (for $2 \leq x/h \leq 6$). Further downstream of the stenosis, the TKE decays gradually and finally approaches zero where the flow is re-laminarized. It is interesting to point out here that this high level of TKE in the immediate post-stenotic region is closely related to the interaction between two shear layers formed from the top and bottom walls, both of which separate from the stenosis and produce the intense pairwise vortices in the post-stenotic region. Figure 4.14(a) compares the Reynolds number effects on the TKE. As expected, as the Reynolds number increases, the TKE level increases in the region immediately downstream of the stenosis where turbulence is just triggered by the stenosis. However, in the far downstream region of the stenosis, where turbulence is significantly damped, the Reynolds number effects on the TKE vanishes. Figure 4.14(b) shows the influence of the stenosis contraction on the TKE. Obviously, as the channel becomes narrower, the stenosis triggers more severe turbulence.

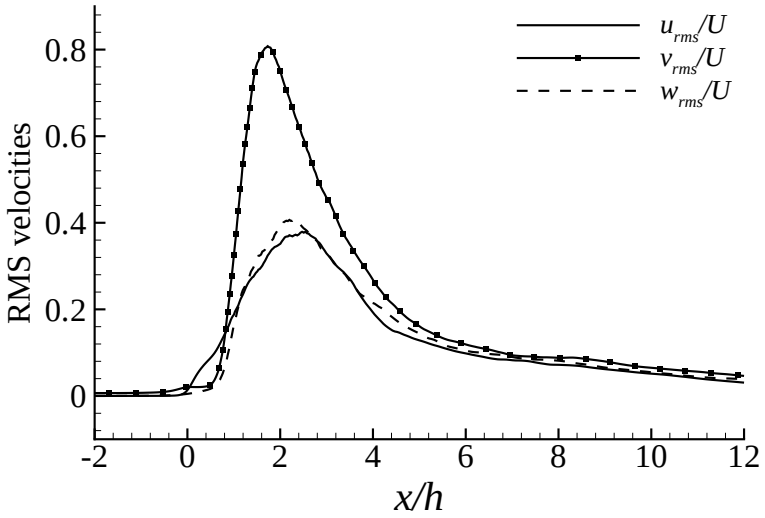

FIGURE 4.15: Non-dimensionalized profiles of the RMS velocities at $y/h = 0.5$ for $Re = 2000$.

4.4.5 Root Mean Square Velocities

Figure 4.15 shows non-dimensionalized profiles of the RMS velocities $u_{rms} \stackrel{\text{def}}{=} \langle u''^2 \rangle^{1/2}$, v_{rms} and w_{rms} (defined similarly) along the central streamline of the domain ($y/h = 0.5$). As shown in Fig. 4.15, the value of u_{rms}/U, v_{rms}/U and w_{rms}/U are very close to zero at the inlet, reflecting the nature of the laminar pulsatile flow pattern in the upstream region. However, after the centre of the stenosis, the RMS values of the velocities begin to increase and become prominent in the immediate post-stenotic region ($0 < x/h < 6$). This physical feature is related to the recirculation flow pattern in the post-stenotic region. Far downstream of the stenosis ($x/h > 6$), the flow is still turbulent but the intensity decreases gradually. The effects of the Reynolds number on the RMS velocities in the upstream region ($x/h < 0$) of the stenosis is indistinctive. However, in the immediate post-stenotic region where the turbulence level is enhanced due to the stenosis, the Reynolds number effects are evident. Figures 4.16(a), 4.16(b), and 4.16(c) show that the magnitude of the RMS velocities increases with the Reynolds number. Figures 4.17(a), 4.17(b), and 4.17(c) show that the magnitude of the RMS velocities increases as the channel becomes narrower.

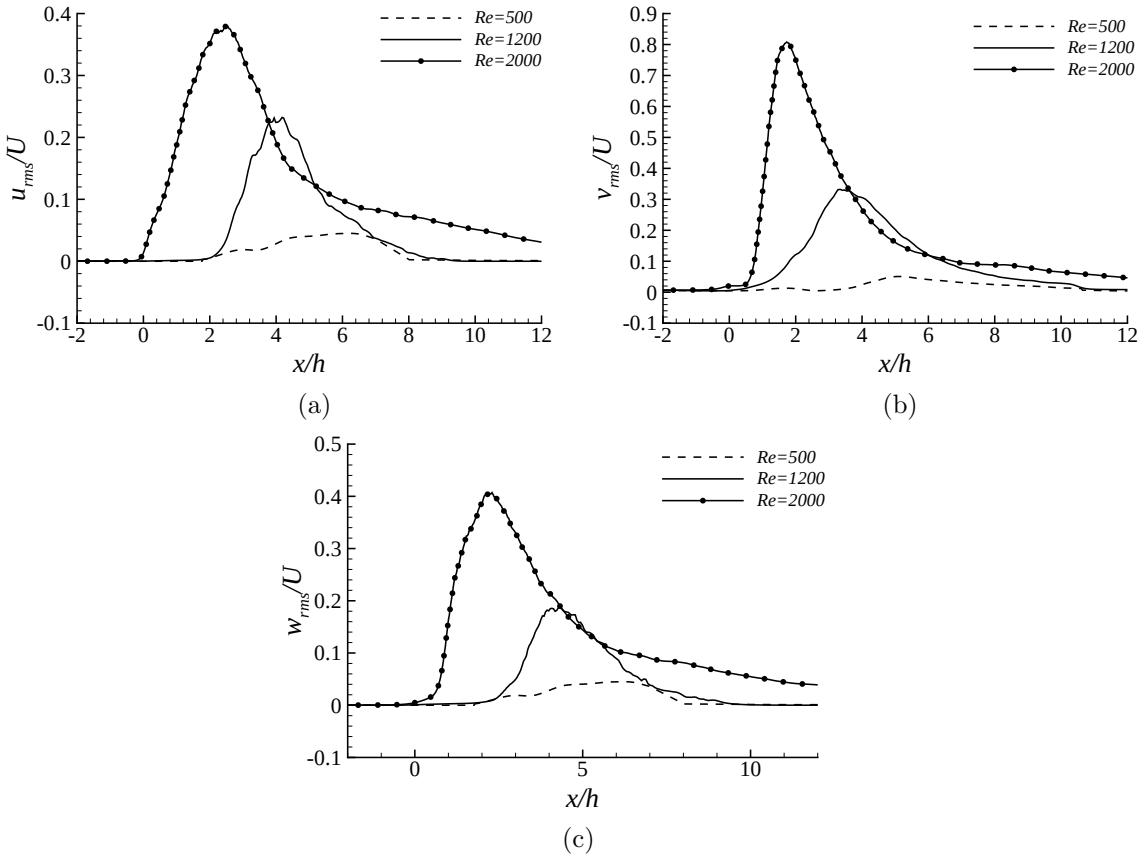

FIGURE 4.16: Non-dimensionalized profiles of the RMS velocities at $y/h = 0.5$ for different Reynolds numbers: (a) u_{rms}/U, (b) v_{rms}/U, and (b) w_{rms}/U.

4.4.6 Energy Spectra

In Fig. 4.18, the non-dimensionalized energy spectra $E_{u''u''} = E(f_s)U/h$ are plotted with respect to the Strouhal number $Sr = f_s h/U$. Here, $E(f_s)$ is the spectra of the square of streamwise velocity fluctuations, u''^2/U^2, extracted based on phase-averaging over the last three pulsatile cycles, and f_s is the time frequency of eddy motions at a specific streamwise location. The frequency spectra is computed using a fast Fourier transform (FFT) scheme. In order to demonstrate the changes in the slope of the energy spectrum, two straight lines corresponding to $(Sr)^{-5/3}$ and $(Sr)^{-10/3}$ are included in Fig. 4.18. According to Tennekes and Lumley [52], a frequency spectrum often includes three distinct subranges. The first subrange contains the energy of the injected flow at very small time frequencies (spatially, corresponding to large-scale eddy motions). The second part is the so-called inertial subrange where the energy

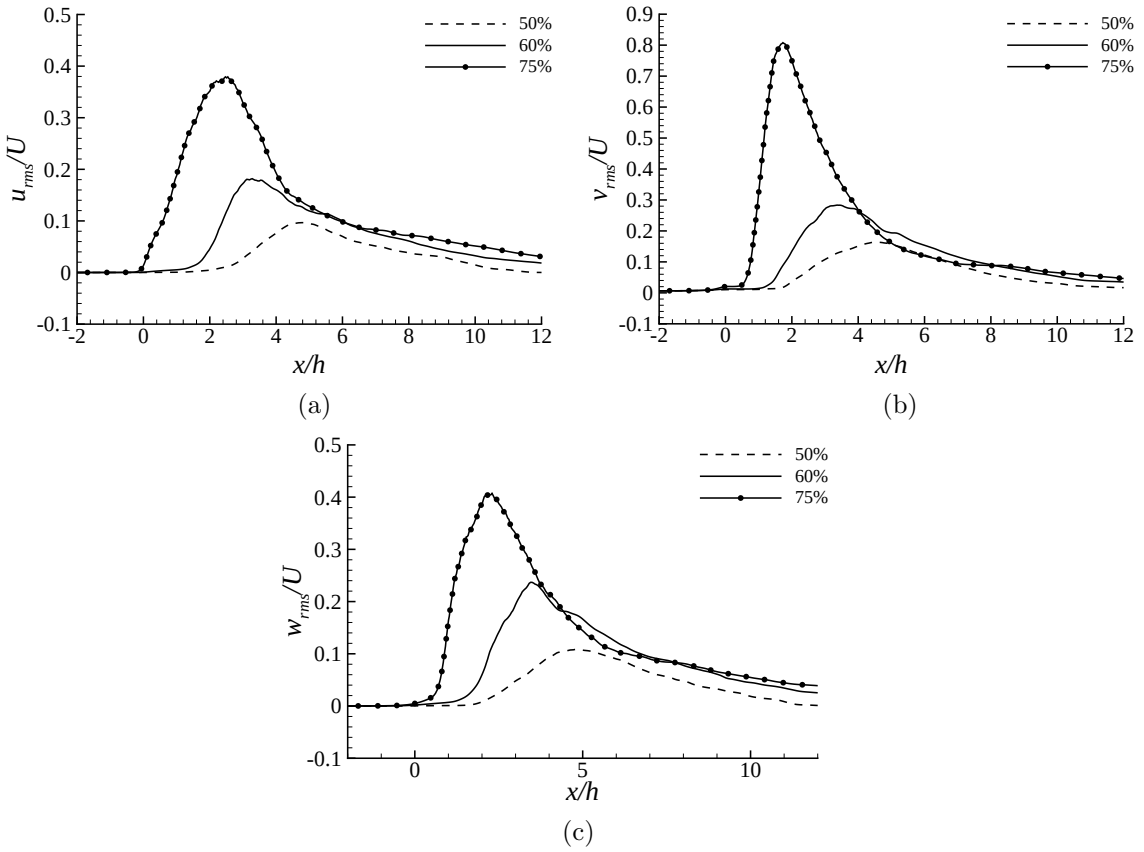

FIGURE 4.17: Non-dimensionalized profiles of the RMS velocities for different degrees of stenoses: (a) u_{rms}/U, (b) v_{rms}/U, and (c) w_{rms}/U.

cascade conserves across each frequency and the spectrum slope is characterized by a constant value, $-5/3$, following the well-known"Kolmogorov's $-5/3$ law". Finally, the third part is the viscous dissipation subrange corresponding to high-frequency turbulent motions (spatially, corresponding to small-scale eddy motions).

In Fig. 4.18(a), it is shown that prior to the stenosis ($x/h = -2$), the slope of the spectrum deviates from the value $-5/3$, which is the characteristic of the inertial subrange. This physical feature is expected, because in the upstream region, the flow is not only laminar but also influenced by the pulsations. This feature of the spectrum slope extends to the centre of the slope ($x/h = 0$), where the flow is still laminar and the onset of turbulence is just triggered due to the constriction of the channel. The signature of the inertial subrange is evident in Figs. 4.18(c)-(f), which correspond to the fully turbulent region in the immediate post-stenotic region

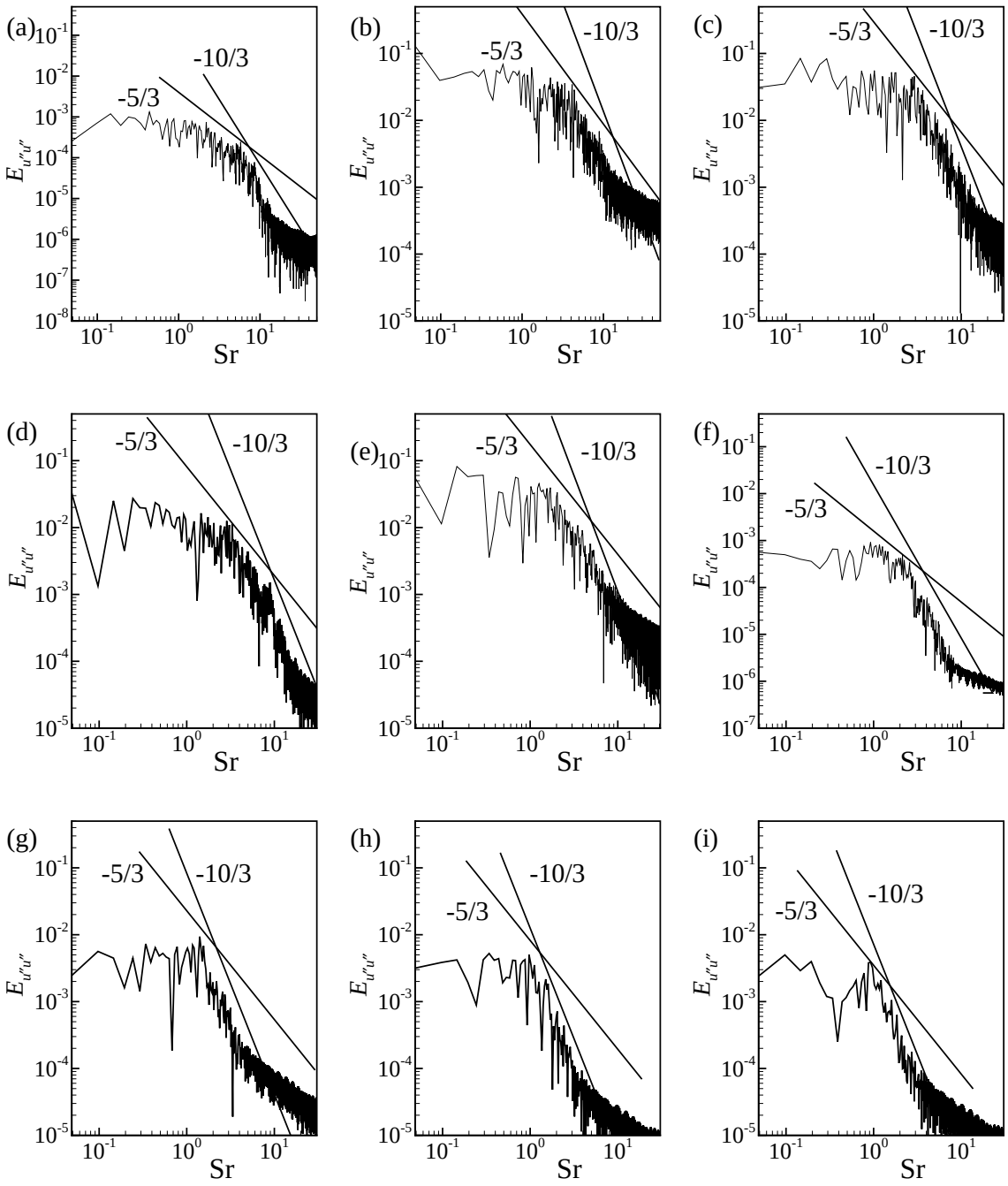

FIGURE 4.18: Non-dimensionalized energy spectrum related to the streamwise fluctuations u'' at the different streamwise locations: (a) $x/h = -2$, (b) $x/h = 0$, (c) $x/h = 2$, (d) $x/h = 3$, (e) $x/h = 4$, (f) $x/h = 5$, (g) $x/h = 6$, (h) $x/h = 8$, and (i) $x/h = 10$.

$(1 \leq x/h \leq 5)$. As shown in Figs. 4.18(g)-(i), in the far downstream region of the stenosis, the interval of the inertial subrange reduces as the turbulent fluctuations decrease due to the re-laminarization tendency. Furthermore, it is observed that the

slope of the spectrum changes from $-5/3$ to $-10/3$ at the higher Strouhal number, which pattern is consistent with the results of Lu *et al.* [62]. In the viscous dissipation subrange, the TKE eventually converts into thermal energy through the mechanism of molecular dissipation.

4.5 Summary of the Chapter

DNS has been performed to investigate physiological pulsatile flow with a Newtonian fluid through a 3D channel with both sided stenosis. The results are presented in various forms to show the effects of stenosis on the turbulent statistics of the velocity field. In the region upstream of the stenosis, the viscous forces are dominant and the flow pattern is primarily laminar. Due to the presence of the stenosis, the wall shear stress increases significantly and wall pressure decreases drastically. Immediately after the stenosis, the flow transits from laminar to turbulent flow patterns. The flow recirculates and an adverse streamwise pressure gradient exists near the upper and lower walls. Furthermore, the turbulent intensity and stresses of the flow increase significantly in the immediate post-stenotic region, however, the turbulence level drops quickly in the streamwise direction and the flow eventually becomes relaminarized in the region far downstream of the stenosis.

Based on the analysis of results for tested cases, it is understood that turbulent fluctuations are highly dependent upon the following physical factors: (i) the presence of the stenosis, which is directly responsible for triggering turbulence and enhancing the RMS velocity levels; (ii) the degree of the stenosis, which controls the cross-sectional area of the throat of the stenosis and significantly influences the turbulence level in the post-stenotic region; and (iii) the Reynolds number, which reflects the acceleration of the flow to turbulence due to the mean driving inertial forces (associated with the mean pressure gradient in the streamwise direction) against the viscous forces (which suppress turbulence through viscous dissipation).

Chapter 5

DNS of a Physiological Pulsatile Non-Newtonian Flow in a Model Arterial Stenosis

5.1 Introduction

Pulsatile laminar-turbulent transitional non-Newtonian fluid flow in a 3D constricted channel represents a challenging topic and has many important applications in biofluids engineering. Human blood flow can be treated as a Newtonian fluid in large arteries, however, in smaller arteries and veins, it behaves typically as a non-Newtonian incompressible viscoelastic fluid [63]. According to Berger and Jou [64], if the shear rate is greater than 100 s^{-1}, the blood behaves like a Newtonian fluid and its viscosity approaches an asymptotic value, $\mu_\infty = 3.45 \times 10^{-3}$ Pa $\cdot$ s. However, if the shear rate of a blood flow falls below this threshold, its viscosity increases and non-Newtonian fluid behaviors begin to exhibit. In this chapter, direct numerical simulations have been conducted to investigate a pulsatile non-Newtonian flow in the context of a channel with 60% stenosis. For the pulsatile flow studied, the Womersley number is set to 10.5 and Reynolds number is set to 1500, both of which are the characteristic of human arterial blood flows. The non-Newtonian flow simulation results are compared against those obtained based on the Newtonian fluid assumption under the same test conditions.

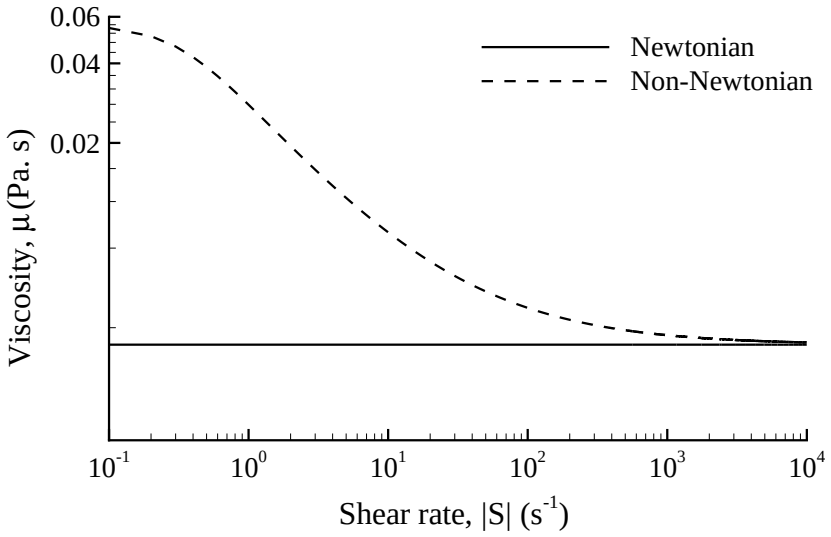

FIGURE 5.1: Relationship between the shear rate and the apparent viscosity for Newtonian and non-Newtonian fluids.

5.2 Non-Newtonian Blood Viscosity Model

The assumption of the Newtonian behavior of blood is limited to high shear rate flow through larger arteries. If the shear rate is below 100 s^{-1}, blood behaves as non-Newtonian fluid (Berger and Jou [64]). The conventional model of Carreau [42] estimates the non-Newtonian viscosity as

$$\mu = \mu_\infty + (\mu_0 - \mu_\infty)[1 + (\lambda|S|)^2]^{\frac{n-1}{2}} \tag{5.1}$$

where μ is the viscosity, $\mu_\infty = 3.45\times10^{-3}$ Pa $\cdot$ s, $\mu_0 = 0.056$ Pa $\cdot$ s is the blood viscosity at zero shear rate, $\lambda = 3.131$ is the time constant associated with the viscosity (that changes with the shear rate), and $n = 0.3568$. Figure 5.1 demonstrates the functional relationship between the shear rate and the apparent blood viscosity of the Carreau model. In this research, the Carreau model is used exclusively for calculating the molecular viscosity of the non-Newtonian fluid.

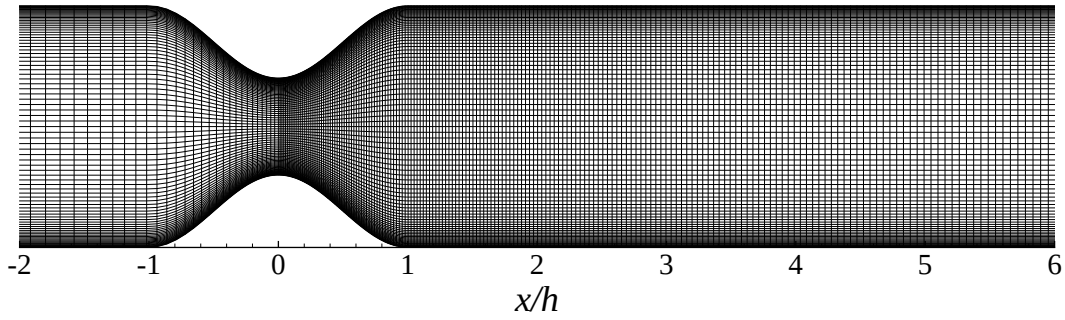

FIGURE 5.2: Schematic of mesh configuration in x-y plane with 60% degree of stenosis.

5.3 Test Case and Mesh Configurations

The arterial stenosis is simplified as a 3D channel with a symmetric cosine-shaped stenosis on the upper and lower walls. The parameters have been explained earlier in chapter 4. In this chapter, f_c is fixed to $\frac{3}{5}$, which results 60% reduction of the cross-sectional area at the centre of the stenosis. In Fig. 5.2, a portion of the mesh configuration is shown in the x-y plane. The results presented in this section is produced using Reynolds number, $Re = 1500$ with $350 \times 90 \times 90$ control volumes (in the stream, vertical and spanwise directions, respectively).

5.4 Inflow Boundary Condition

The real part of the solution of Eq. (2.8) is used as an inlet boundary condition to generate the pulsatile flow. For $Re = 1500$, the value of A is set to 0.35. The inlet pulsatile velocity profile derived from Eq. (2.8) is very similar to that shown in Fig. 4.2, and therefore, is not presented here in order to keep the discussion concise.

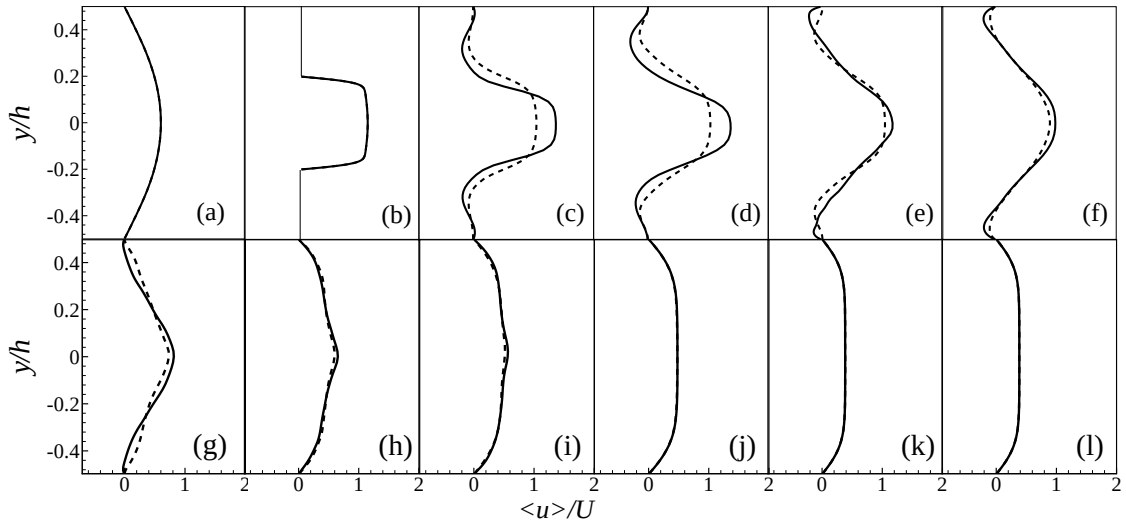

FIGURE 5.3: The mean streamwise velocity $\langle u \rangle / U$ at (a) $x/h = -5.0$, (b) $x/h = 0.0$, (c) $x/h = 1.0$, (d) $x/h = 2.0$, (e) $x/h = 3.0$, (f) $x/h = 3.5$, (g) $x/h = 4.0$, (h) $x/h = 5.0$, (i) $x/h = 6.0$, (j) $x/h = 8.0$, (k) $x/h = 10.0$, and (l) $x/h = 15.0$ (solid line for the Newtonian flow, and dashed line for the non-Newtonian flow).

5.5 Results and Analysis

5.5.1 Flow Characteristics

Figures 5.3 and 5.4 compare the mean streamwise velocity u (non-dimensionalized using the bulk velocity U) and the non-dimensionalized time- and spanwise-averaged TKE, k, respectively, for the Newtonian and non-Newtonian cases at different streamwise locations. The pulsatile inlet condition and the stenosis jointly trigger a laminar-turbulent-laminar transition in the streamwise direction. In addition, the flow separates after the stenosis forming two distinctive recirculation regions. In both the Newtonian and non-Newtonian cases, the flow velocity reaches its maximum value at the centre of the stenosis. Immediately downstream of the throat of the stenosis ($x/h = 0$), the flow becomes turbulent and then gradually re-laminarizes in the far downstream region ($x/h > 6$). Further downstream the flow continues to develop. From Fig. 5.3, it can be seen that mean streamwise velocity is slightly higher for Newtonian flow than that for non-Newtonian flow, especially in the region immediately downstream of the stenosis.

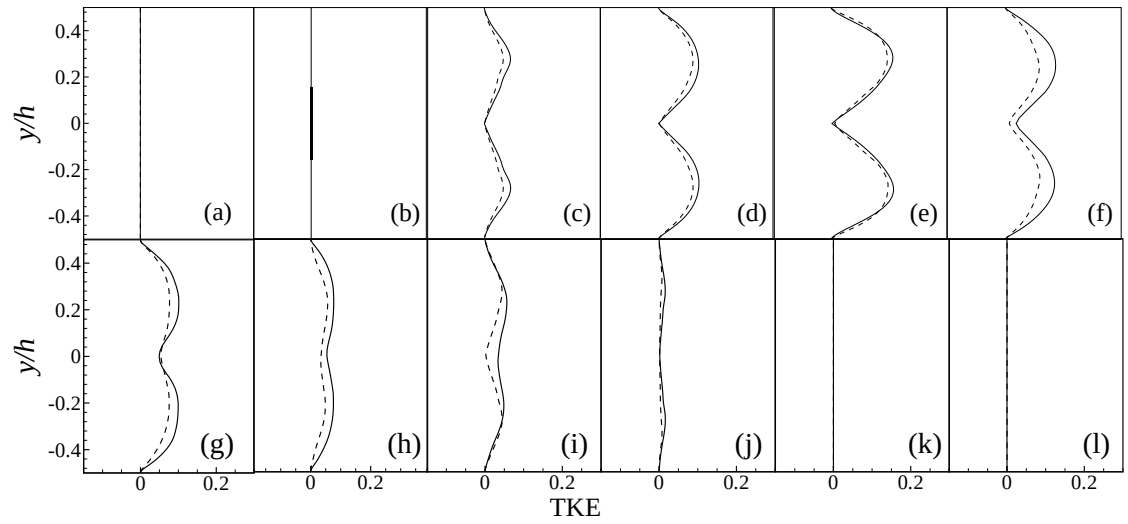

FIGURE 5.4: Non-dimensionalized time- and spanwise-averaged profile of TKE k/U^2 at (a) $x/h = -5.0$, (b) $x/h = 0.0$, (c) $x/h = 1.0$, (d) $x/h = 2.0$, (e) $x/h = 3.0$, (f) $x/h = 3.5$, (g) $x/h = 4.0$, (h) $x/h = 4.5$, (i) $x/h = 5.0$, (j) $x/h = 6.0$, (k) $x/h = 10.0$, and (l) $x/h = 15.0$ (solid line for the Newtonian flow, and dashed line for the non-Newtonian flow).

Figure 5.5 illustrates the contours of the instantaneous streamwise velocity at the central vertical plane ($z/h = 1.5$) at $Re = 1500$ for the non-Newtonian flow. The time-averaged vortical structures of the flow are visualized using the contours of non-dimensionalized mean streamwise velocity. Two distinct recirculation regions appear near the post-lip of the stenosis due to the separation of the shear layer induced by the stenosis.

Figure 5.6 shows the slice view of the isopleths of the non-dimensionalized instantaneous streamwise velocity field u/U at $t/T = 10.25$. The flow entering the stenosis accelerates while remaining laminar and stratified. Immediately downstream of the throat of the stenosis, the flow separates from the upper and lower surfaces but remains stratified. Further downstream ($x/h > 1$) there is a transition to fully 3D flow. Finally, the flow re-laminarizes (see the last four slices in Fig. 5.6), the flow re-establishes a stratified profile.

In Fig. 5.7, the cycle-to-cycle flow development is shown using the contour plots of the streamwise velocity u (non-dimensionalized using the bulk velocity U) for non-Newtonian flow. A snapshot of the contours is made for the instantaneous streamwise

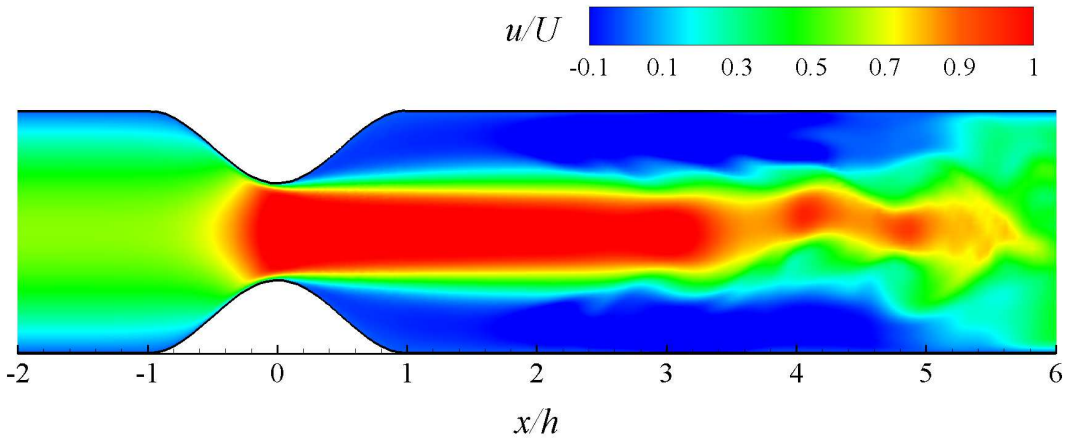

FIGURE 5.5: Contour of the instantaneous streamwise velocity u/U at $t/T = 10.25$ for non-Newtonian flow.

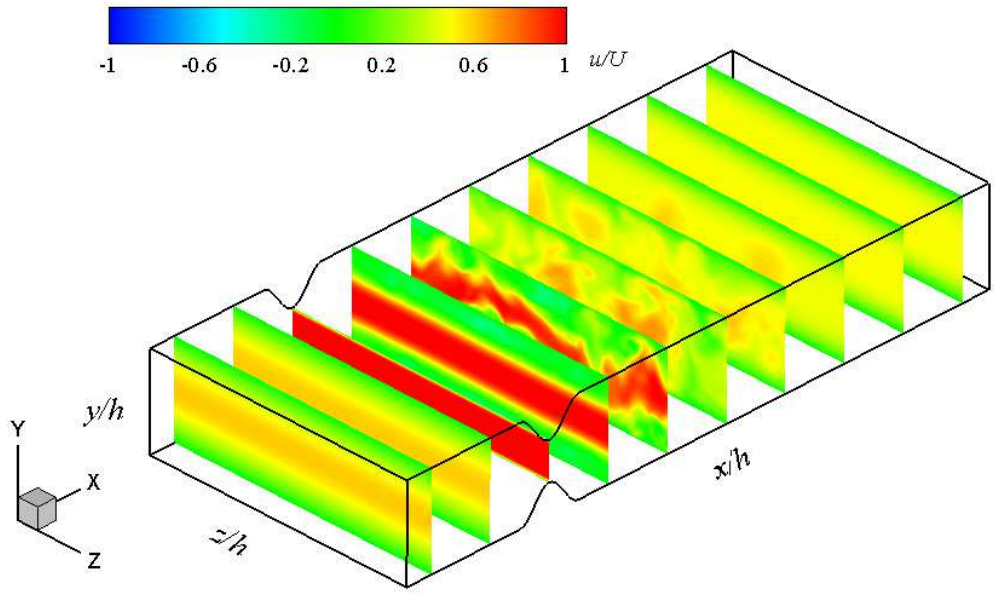

FIGURE 5.6: Slice view of instantaneous streamwise velocity u/U at $t/T = 10.25$ for the non-Newtonian flow.

velocity at the end of each cycle for $Re = 1500$. The simulation has been carried out up to the end of the tenth cycle. It has been confirmed that the solutions eventually reach a stationary state after the eighth cycle, and the flow statistics accumulated after the eighth cycle do not vary significantly between the eighth and tenth cycles. As shown in Fig. 5.7(a), at the end of the first cycle, it is observed that two small recirculation regions near the two walls are generated. As shown in Fig. 5.7(b), a primary shear layer which is initially created at the centre of the stenosis propagates

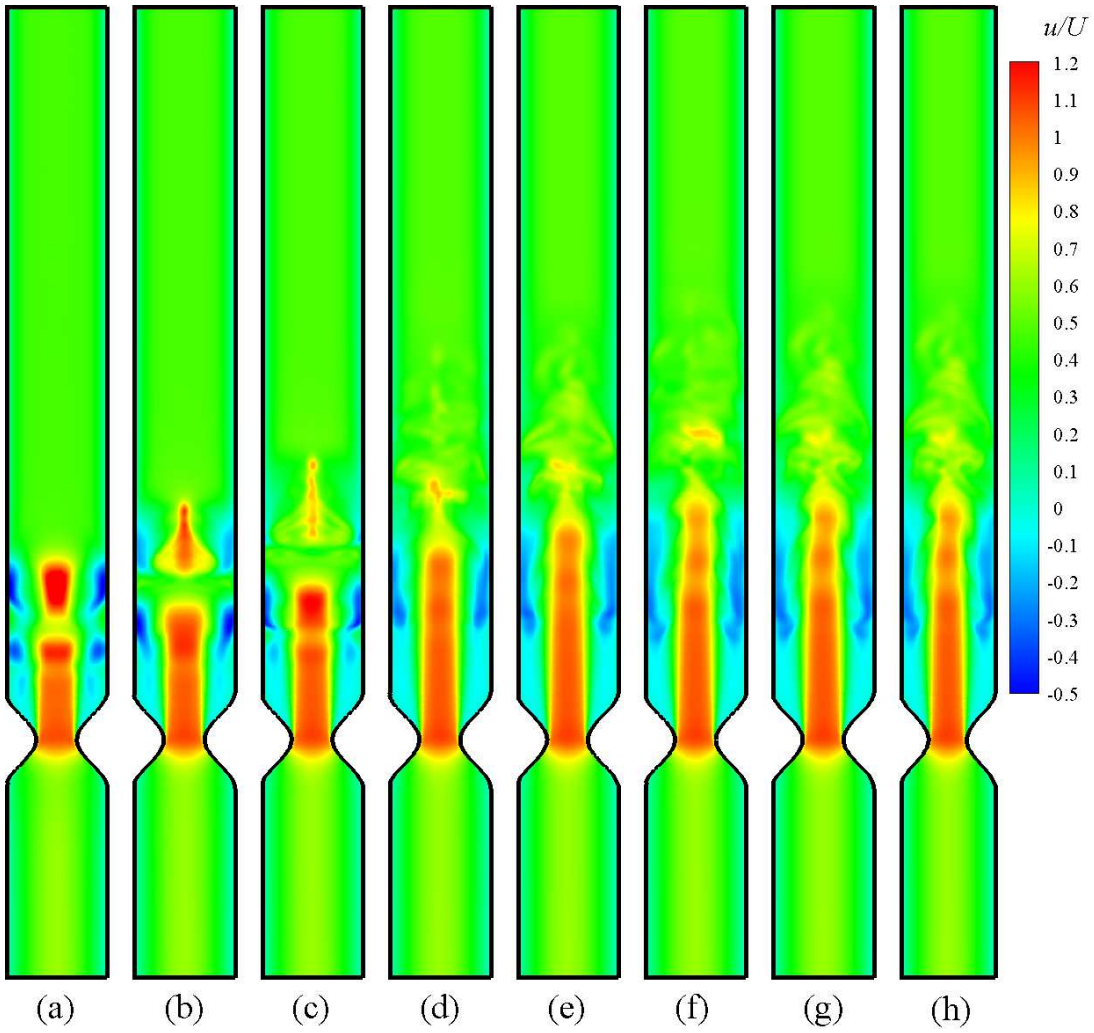

FIGURE 5.7: Contours of streamwise velocity u/U at: (a) $t/T = 1.25$, (b) $t/T = 3.25$, (c) $t/T = 5.25$, (d) $t/T = 6.25$, (e) $t/T = 7.25$, (f) $t/T = 8.25$, (g) $t/T = 9.25$ and (h) $t/T = 10.25$ for the non-Newtonian flow at $Re = 1500$.

towards the downstream region at the end of the second cycle. As the flow field evolves with time, the shear layers elongate and finally break down into vortices that eventually induce the flow a fully turbulent state immediately after the stenosis (see Figs. 5.7(c)-(h)).

5.5.2 Wall Shear Stresses

Figures 5.8 (a) and (b) display the averaged and instantaneous profile of the wall shear stress $\tau_w = \mu \frac{\partial u}{\partial y}|_w$ (non-dimensionalized using $\frac{1}{2}\rho U^2$) over the upper and lower

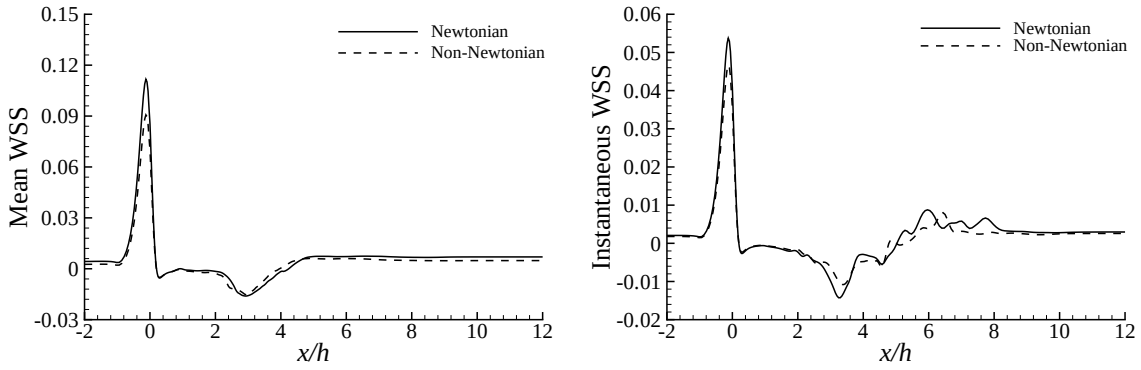

(a) (b)

FIGURE 5.8: Non-dimensionalized profile of the wall shear stress (a) time- and spanwise-averaged, $\langle \tau_w \rangle / \frac{1}{2}\rho U^2$, and (b) instantaneous, $\tau_w / \frac{1}{2}\rho U^2$.

walls for both the non-Newtonian and Newtonian cases. The wall shear stress for the non-Newtonian case is lower than that for the Newtonian case over most of the channel due to the higher predicted local viscosity by the Carreau viscosity model. The wall shear stress rises rapidly at the throat location and then drops sharply in the post-stenotic region where the flow separates. Within $0 < x/h < 6$, the wall shear stress becomes negative due to the recirculation of the flow adjacent to the wall, and then slightly rises to an approximately constant small finite value in the further downstream region. For the non-Newtonian flow case, the wall shear stress is slightly higher close to the re-attachment point.

5.5.3 Wall Pressure

Figure 5.9 illustrates the contour of the non-dimensionalized time- and spanwise-averaged wall pressure $\langle p \rangle / \rho U^2$ in the central vertical plane ($z/h = 1.5$) and Fig. 5.10 shows the non-dimensionalized time- and spanwise-averaged wall pressure distribution along the streamwise direction of the flow. As evident in both figures, owing to the constriction of the channel, the wall pressure drops significantly at the centre of the stenosis. As shown in Figs. 5.9 and 5.10, the maximum pressure drop occurs in the immediate post-stenotic region for $0 < x/h < 3$, where an adverse pressure gradient presents and flow recirculates. From Fig. 5.10, it is evident that the maximum wall

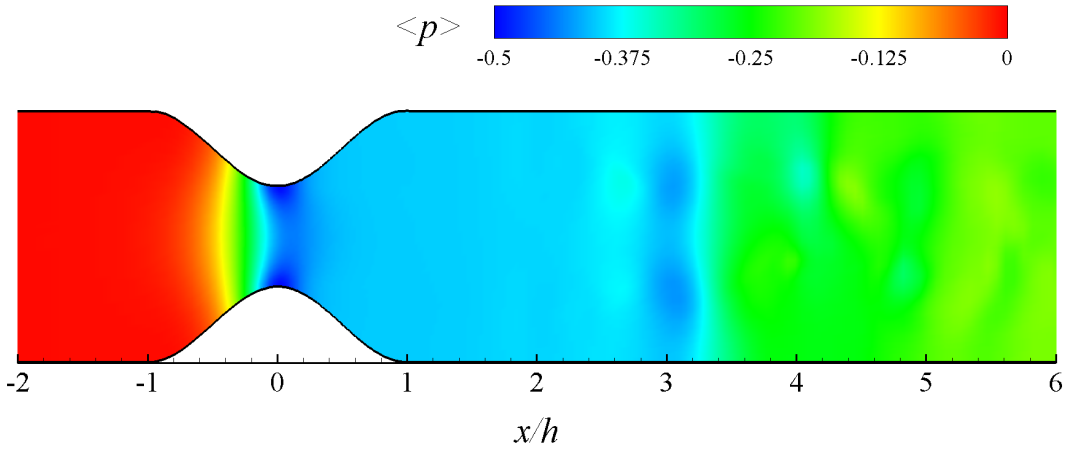

FIGURE 5.9: Contours of non-dimensionalized time- and spanwise-averaged wall pressure, $\langle p \rangle / \rho U^2$ for the non-Newtonian flow.

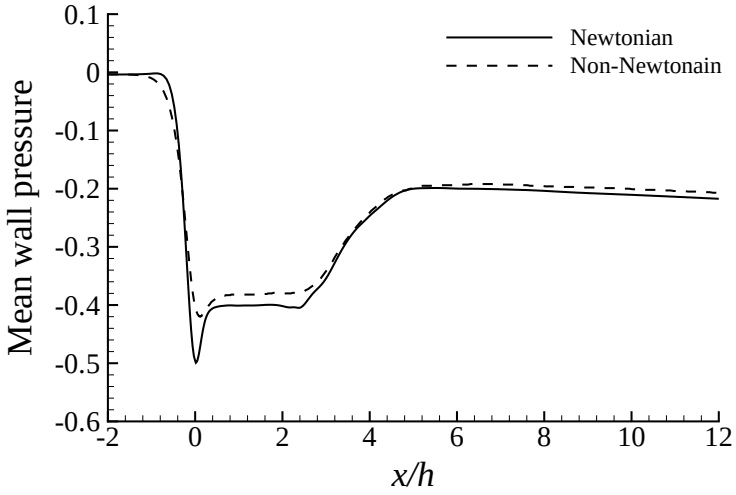

FIGURE 5.10: Non-dimensionalized time- and spanwise-averaged profiles of wall pressure $\langle p \rangle / \rho U^2$ for the Newtonian and the non-Newtonian flows.

pressure drop is higher for the Newtonian flow than for the non-Newtonian flow. This is because the fluid viscosity as predicted by the Carreau model for the non-Newtonian fluid is higher than the viscosity of the Newtonian fluid. As a result, both pressure and kinematic energy of the flow dissipates faster in the non-Newtonian case.

5.5.4 Turbulence Kinetic Energy

Figure 5.11 shows the non-dimensionalized time- and spanwise-averaged TKE k of the flow along the streamwise direction for the Reynolds number 1500. Figure 5.12

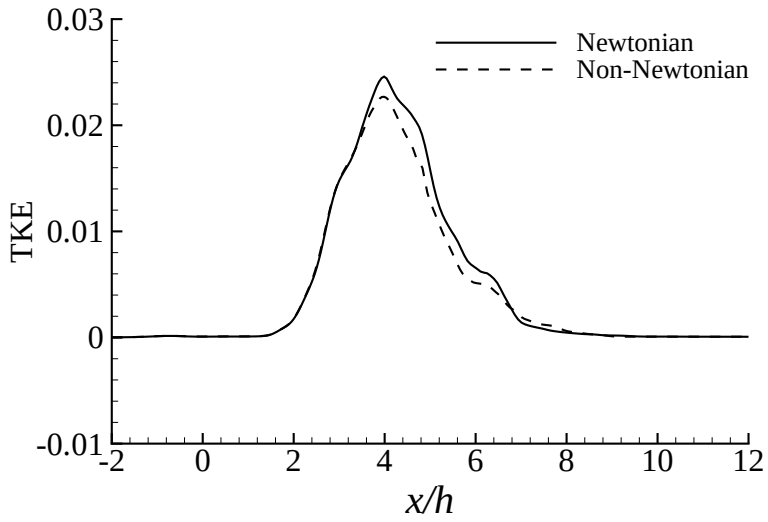

FIGURE 5.11: Non-dimensionalized time- and spanwise-averaged profiles of TKE k/U^2 for the Newtonian and the non-Newtonian flows.

illustrates the contours of the non-dimensionalized time- and spanwise-averaged TKE k in the central vertical plane ($z/h = 1.5$). Figure 5.11 compares the effects of viscosities due to the Newtonian and non-Newtonian fluid assumptions on the prediction of the TKE. In the turbulent region (for $1 \leq x/h \leq 6$), the TKE magnitude for the non-Newtonian flow is slightly lower than that of the Newtonian flow. As shown in the figure 5.11, for both Newtonian and non-Newtanian fluids, the flow is fully laminar as it is evident that $k = 0$ holds upstream of the stenosis. As soon as the flow passes the centre of the stenosis, turbulence is triggered and the TKE starts to increase rapidly and reaches its maximum value in the immediate post-stenotic region ($1 \leq x/h \leq 6$). However, the TKE decays gradually in the far downstream region and finally becomes trivial where the flow is re-laminarized.

5.5.5 Root Mean Square Velocities

Figure 5.13(a) shows non-dimensionalized profiles of the RMS velocities u_{rms}, v_{rms} and w_{rms} along the central streamline of the domain ($y/h = 0.5$). As shown in Fig. 5.13(a), the value of u_{rms}/U, v_{rms}/U and w_{rms}/U are very close to zero at the inlet, reflecting the nature of the laminar pulsatile flow pattern in the upstream region. However, after the centre of the stenosis, the RMS values of the velocities begin to

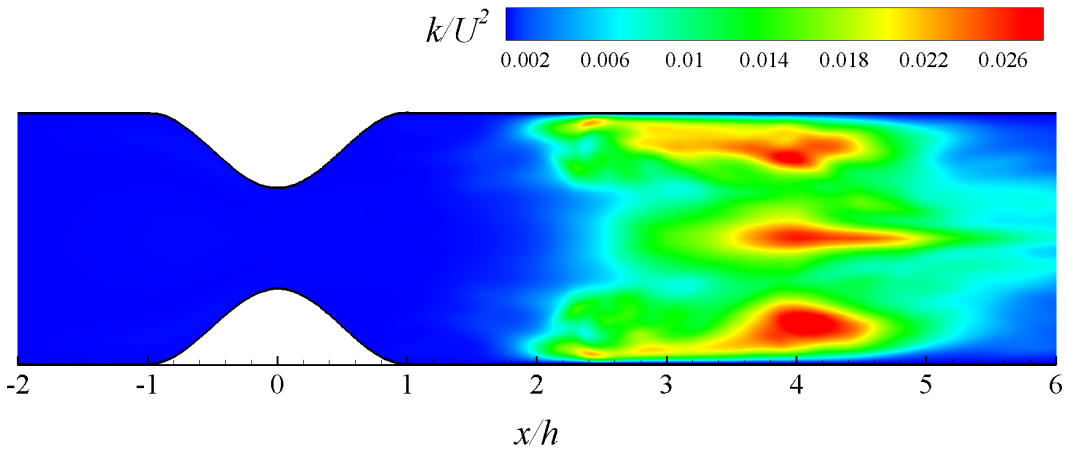

FIGURE 5.12: Contour of non-dimensionalized time- and spanwise-averaged TKE k/U^2 for the non-Newtonian flow.

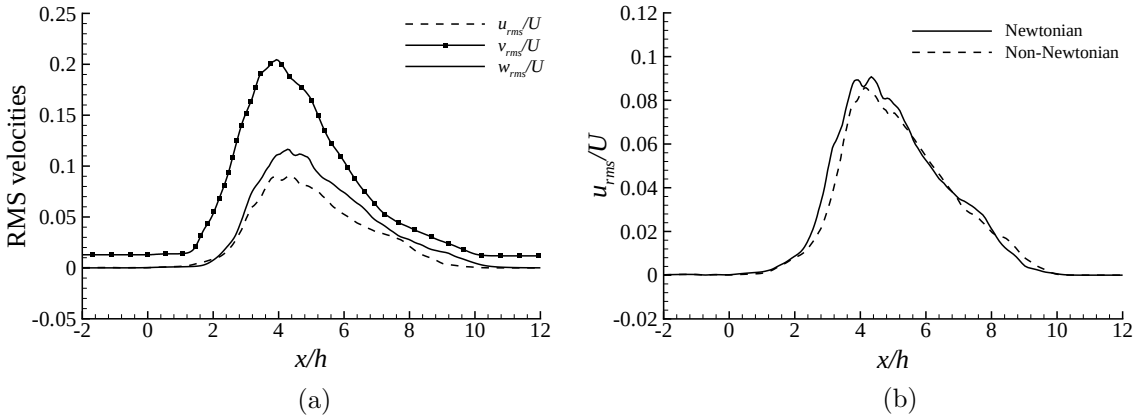

FIGURE 5.13: Non-dimensionalized profiles of the RMS velocities at $y/h = 0.5$; (a) u_{rms}/U, v_{rms}/U, and w_{rms}/U for the non-Newtonian flow and (b) u_{rms}/U for the Newtonian and the non-Newtonian flows.

increase and become prominent in the immediate post-stenotic region ($1 < x/h < 6$). This physical feature is related to the recirculation flow pattern in the post-stenotic region. Far downstream of the stenosis ($x/h > 6$), the flow is still turbulent but the intensity decreases gradually. In general, the profiles of RMS velocity exhibited here are similar to the TKE profiles discussed previously in Fig. 5.13(a). Furthermore, Fig. 5.13(b) shows that the magnitude of the streamwise RMS velocity is slightly lower for the non-Newtonian flow than that for the Newtonian flow.

5.5.6 Energy spectra

Figure 5.14 shows non-dimensionalized energy spectra $E_{u''u''}$ with respect to the Strouhal number Sr calculated based on the non-Newtonian blood viscosity model of Carreau [42]. As shown in Fig. 5.14(a), the slope of the spectrum deviates from the value $-5/3$ (which is a characteristic of the inertial subrange) prior to the stenosis ($x/h = -2$). For this test case, the flow is not only laminar but also influenced by the pulsations in the upstream region. This observed physical feature is expected as the first subrange contains the energy of the injected flow at very small time frequencies (Tennekes and Lumley [52]). This feature of the spectrum slope extends to the centre of the slope ($x/h = 0$), where the flow is still laminar and the onset of turbulence is just triggered due to the constriction of the channel. In the immediate post-stenotic region ($1 \leq x/h \leq 5$), the signature of the inertial subrange is evident in Figs. 5.14(b)-(f), which correspond to the fully turbulent region. In the far downstream region of the stenosis, the interval of the inertial subrange reduces as the turbulent fluctuations decrease due to the re-laminarization tendency (see Figs. 5.14(g)-(i)). Furthermore, the slope of the energy spectra changes from $-5/3$ to $-10/3$ at higher Strouhal numbers. The change in the spectrum slope in the far downstream region of the stenosis is a consequence of the re-laminarization process, where the viscous dissipation subrange is predominant and the kinetic energy dissipates due to the effects of viscosity.

5.6 Summary of the Chapter

Non-Newtonian physiological flow in a model arterial stenosis has been investigated by using DNS. When the shear rate of the blood flow is less than $100s^{-1}$, it becomes necessary to activate the non-Newtonian blood viscosity model in numerical simulations. It is observed in this research that the flow characteristics are apparently altered from the Newtonian flow behaviors once the non-Newtonian viscosity model is activated. In this research, a high Womersley number ($\alpha = 10.5$) and a low Reynolds

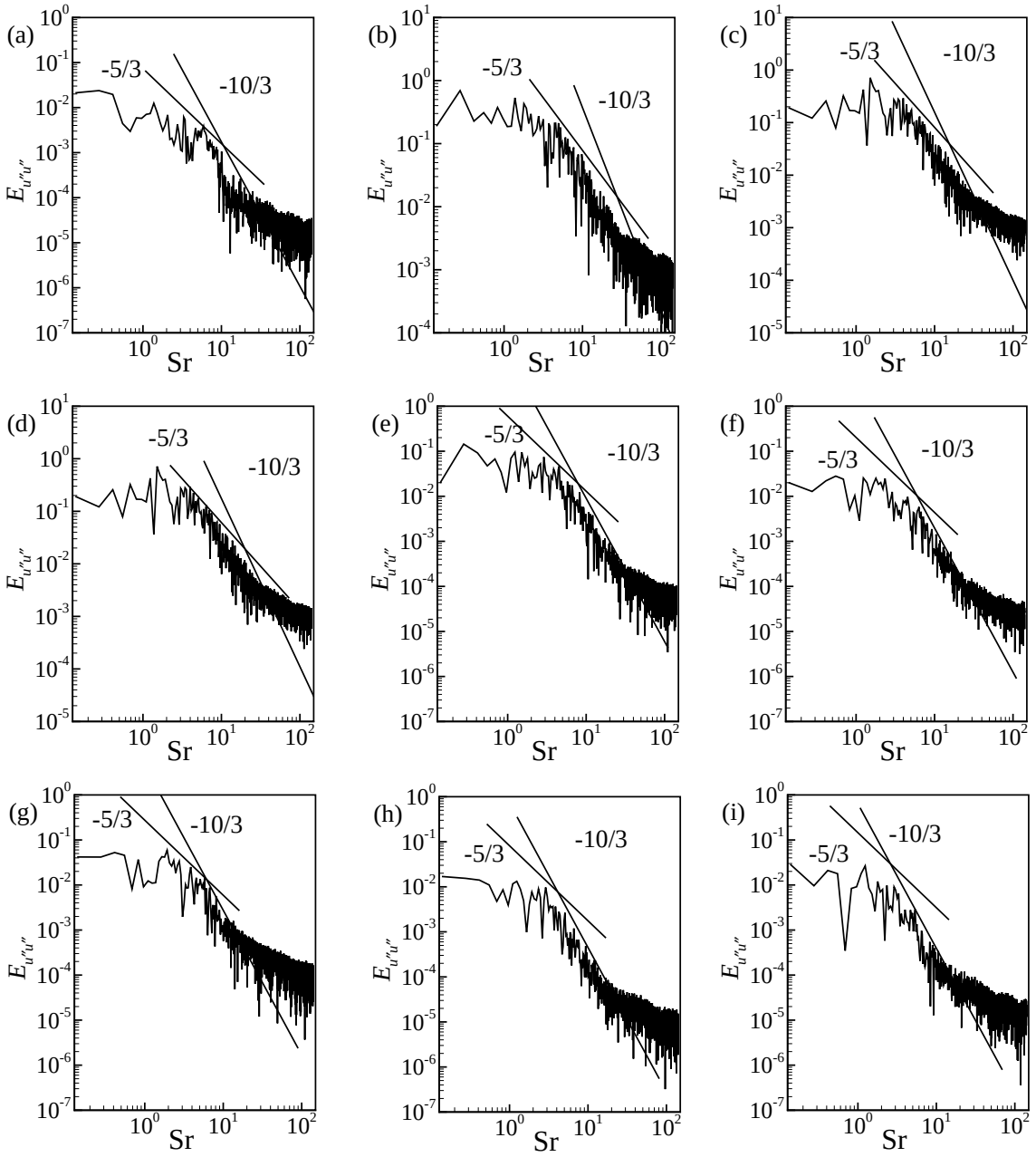

FIGURE 5.14: Non-dimensionalized energy spectrum related to the streamwise fluctuations u'' at the different streamwise locations: (a) $x/h = -2$, (b) $x/h = 0$, (c) $x/h = 2$, (d) $x/h = 3$, (e) $x/h = 4$, (f) $x/h = 5$, (g) $x/h = 6$, (h) $x/h = 8$, and (i) $x/h = 10$.

numbers ($Re = 1500$) were tested, which are characteristics of blood flows in the arteries of humans and animals. In comparison with the Newtonian flow behavior, for the non-Newtonian flow, the mean streamwise velocity is slightly smaller and the streamwise extent of the recirculation region is slightly longer. In general, the

wall shear stress for the non-Newtonian case is lower than that for the Newtonian case. In the immediate post-stenotic region, the pressure drops sharply due to the sudden acceleration of the flow, and the predicted pressure drop is smaller for the non-Newtonian flow. As soon as the flow passes the centre of the stenosis, turbulence is triggered and the TKE starts to increase rapidly and reaches its maximum value in the immediate post-stenotic region ($1 \leq x/h \leq 6$). The TKE magnitude predicted by the Carreau model for the non-Newtonian fluid flow is slightly lower than that for the Newtonian flow due to fact that the viscous dissipation level is slightly higher in the non-Newtonian flow.

Chapter 6

Conclusions and Future Work

6.1 Conclusions

DNS has been performed to investigate physiological pulsatile flow through a 3D channel with both sided cosine-shaped stenosis. The physics of the physiological pulsatile flow under investigation is dominated by three major factors, the pulsatile inertial forces (as a consequence of the pulsatile inlet boundary condition), the mean driving inertial forces (associated with the mean pressure gradient in the streamwise direction), and the geometry of the stenosis. Owing to the narrowing of the channel, transition of the pulsatile flow from laminar to turbulent pattern occurs immediately downstream of the stenosis, and the flow becomes re-laminarized in the far downstream region of the stenosis. The transition-to-turbulence of the flow is directly triggered by the stenosis, which however, is further complicated by the pulsatile inertial forces and the mean driving inertial forces. Both the pulsatile inertial forces and the mean driving inertial forces tend to enhance turbulence and flow unsteadiness, and the effects of these two types of forces in comparison with the viscous forces (which tend to suppress turbulence) can be quantified using the Womersley number and Reynolds number, respectively. For the Newtonian flow, a high Womersley number ($\alpha = 10.5$) and three low Reynolds numbers ($Re = 500, 1200$ and 2000) were tested.

The results of pulsatile Newtonian flows are presented in various forms to show

the effects of stenosis on the turbulent statistics of the velocity field. In the region upstream of the stenosis, the flow pattern is primarily laminar. Therefore, the wall shear stresses are very close to zero. Due to the presence of the stenosis, the wall shear stress increases significantly and wall pressure decreases drastically. Immediately after the stenosis, the flow recirculates and an adverse streamwise pressure gradient exists near the walls. Furthermore, the turbulent intensity of the flow increases significantly in the immediate post-stenotic region. It is also observed that the TKE of the flow field is dependent upon the Reynolds number and the degree of stenosis of the channel. In the region far downstream of the stenosis, the flow is re-laminarized and the value of these quantities again becomes vanishingly small.

In this research, it is also demonstrated that DNS is a useful predictive tool for numerical study of the transition and pulsation of a non-Newtonian arterial stenotic flow. In general, it is observed in this research that the flow characteristics are apparently altered from the Newtonian flow behaviors once the non-Newtonian viscosity model is activated. A high Womersley number ($\alpha = 10.5$) and a low Reynolds numbers ($Re = 1500$) were tested, which are characteristics of blood flows in arteries of human. The results show that the streamwise velocity and TKE predicted by the non-Newtonian viscosity model are slightly smaller than those predicted by the Newtonian viscosity model. The maximum wall stresses and wall pressure drop in the immediate post-stenotic region are also slightly smaller in the context of the non-Newtonian flow. The TKE magnitude predicted by the Carreau model for the non-Newtonian fluid flow is slightly lower than that for the Newtonian flow due to fact that the viscous dissipation level is slightly higher in the non-Newtonian flow.

6.2 Future Work

This research can be extended to investigate more realistic blood flow through arteries. The following lists the potential research directions for future studies:

- This research considers a modeled stenosis formed between two parallel flat

plates. In future, different types of modeled stenoses can be also considered, based on, e.g. circular tubes of regular and irregular streamwise curvatures.

- The boundary of the modeled stenosis is considered rigid in this study. Given the fact that the arterial walls in real biological system are compliant, future simulation may include nonlinear and elastic boundary materials.

- The modeled stenosis in the channel was formed smoothly using a mathematical function (i.e., cosine curve), which deviates in general from clinical conditions. Back *et al.* [65] suggests that the more realistic biological stenosis wall is often rough rather than smooth. In view of this, stenosis of irregular cross-sectional geometries can be also considered for further investigations.

- In this study, only one single stenosis was considered. Investigation of the effects of multiple stenoses in a single circular tube can be another interesting topic.

References

[1] N. Beratlis, E. Balaras, B. Parvinian, and K. Kiger, "A numerical and experimental investigation of transitional pulsatile flow in a stenosed channel," *ASME J. Biomech. Eng.*, vol. 127, pp. 1147–1157, 2005.

[2] D. N. Ku, "Blood flows in arteries," *Annu. Rev. Fluid Mech.*, vol. 29, pp. 399–434, 1997.

[3] S. S. Varghese, S. H. Frankel, and P. F. Fisher, "Direct numerical simulation of stenotic flows: Part I. Steady flow," *J. Fluid Mech.*, vol. 582, pp. 253–280, 2007.

[4] S. S. Varghese, S. H. Frankel, and P. F. Fisher, "Direct numerical simulation of stenotic flows: Part II. Pulsatile flow," *J. Fluid Mech.*, vol. 582, pp. 281–318, 2007.

[5] K. Bhaganagar, "Direct numerical simulation of flow in stenotic channel to understand the effect of stenotic morphology on turbulence," *J. Turbul.*, vol. 10, pp. 1–16, 2009.

[6] M. C. Paul and M. M. Molla, "Investigation of physiological pulsatile flow in a model arterial stenosis using large-eddy and direct numerical simulations," *Appl. Math. Mod.*, vol. 36 (9), pp. 4393–4413, 2011.

[7] M. M. Molla, B.-C. Wang, and D. C. S. Kuhn, "Numerical study of pulsatile

channel flows undergoing transition triggered by a modelled stenosis," *Phys. Fluids*, vol. 24 (12), p. 121901, 2012.

[8] A. M. A. Khalifa and D. P. Giddens, "Analysis of disorder in pulsatile flows with application to poststenotic blood velocity measurement in dogs," *J. Biomech.*, vol. 11 (3), pp. 129–141, 1978.

[9] A. M. A. Khalifa and D. P. Giddens, "Characterization and evolution of poststenotic flow disturbances," *J. Biomech.*, vol. 14, pp. 279–296, 1981.

[10] S. D. Peterson and M. W. Plesniak, "The influence of inlet velocity profile and secondary flow on pulsatile flow in a model artery with stenosis," *J. Fluid Mech.*, vol. 616, pp. 263–301, 2008.

[11] S. A. Ahmed and D. P. Giddens, "Velocity measurements in steady flow through axisymmetric stenoses at moderate Reynolds numbers," *J. Biomech.*, vol. 16 (7), pp. 505–516, 1983.

[12] S. A. Ahmed and D. P. Giddens, "Flow disturbance measurements through a constricted tube at moderate Reynolds numbers," *J. Biomech.*, vol. 16 (12), pp. 955–963, 1983.

[13] S. A. Ahmed and D. P. Giddens, "Pulsatile poststenotic flow studies with laser Doppler anemometry," *J. Biomech.*, vol. 17 (5), pp. 695–705, 1984.

[14] R. A. Cassanova and D. P. Giddens, "Disorder distal to modeled stenoses in steady and pulsatile flow," *J. Biomech.*, vol. 11 (10-12), pp. 441–453, 1978.

[15] S. A. Ahmed, "An experimental investigation of pulsatile flow through a smooth constriction," *Exp. Therm. Fluid Sci.*, vol. 17 (4), pp. 309–318, 1998.

[16] W. Yongchareon and D. F. Young, "Initiation of turbulence in models of arterial stenosis," *J. Biomech.*, vol. 12 (3), pp. 185–196, 1979.

[17] L. C. Cheng, M. E. Clark, and J. M. Robertson, "Numerical calculations of oscillating flow in the vicinity of square wall obstacles in plane conduits," *J. Biomech.*, vol. 5, pp. 467–484, 1972.

[18] B. J. Daly, "A numerical study of pulsatile flow through stenosed canine femoral arteries," *J. Biomech.*, vol. 9, pp. 465–475, 1976.

[19] V. O'Brien and L. W. Ehrlich, "I. Simple pulsatile flow in an artery with a constriction," *J. Biomech.*, vol. 18, pp. 117–127, 1976.

[20] F. T. Smith, "The separating flow through a severely constricted symmetric tube," *J. Fluid Mech.*, vol. 90 (4), pp. 725–754, 1979.

[21] K. Imaeda and F. O. Goodman, "Analysis of non-linear pulsatile blood flow in arteries," *J. Biomech.*, vol. 13 (12), pp. 1007–1021, 1980.

[22] C. Tu, M. Deville, L. Dheur, and L. Vanderschuren, "Finite element simulation of pulsatile flow through arterial stenosis," *J. Biomech.*, vol. 25 (10), pp. 1141–1152, 1992.

[23] G. R. Zendehbudi and M. S. Moayeri, "Comparison of physiological and simple pulsatile flows through stenosed arteries," *J. Biomech.*, vol. 32 (9), pp. 959–965, 1999.

[24] K. Haldar, "Oscillatory flow of blood in a stenosed artery," *Bull. Math. Biol.*, vol. 49 (3), pp. 279–287, 1987.

[25] S. S. Varghese and S. H. Frankel, "Numerical modeling of pulsatile turbulent flow in stenotic vessels," *ASME J. Biomech. Eng.*, vol. 125, pp. 445–460, 2003.

[26] T. S. Lee, W. Liao, and H. T. Low, "Numerical simulation of turbulent flow through series stenoses," *Int. J. Numer. Meth. Fluids*, vol. 42 (7), pp. 717–740, 2003.

[27] T. S. Lee, W. Liao, and H. T. Low, "Numerical study of physiological turbulent flows through series arterial stenosis," *Int. J. Numer. Meth. Fluids*, vol. 46 (3), pp. 315–344, 2004.

[28] M. X. Li, J. J. Beech-Brandt, L. R. John, P. R. Hoskins, and W. J. Easson, "Numerical analysis of pulsatile blood flow and vessel wall mechanics in different degrees of stenoses," *J. Biomech.*, vol. 40 (16), pp. 3715–3724, 2007.

[29] A. Scotti and U. Piomelli, "Numerical simulation of pulsating turbulent channel flow," *Phys. Fluids*, vol. 13 (5), pp. 1367–1384, 2001.

[30] J. S. Stroud, S. A. Berger, and D. Saloner, "Influence of stenosis morphology on flow through severely stenotic vessels: implications for plaque rupture," *J. Biomech.*, vol. 33, pp. 443–455, 2000.

[31] M. C. Melaaen, "Analysis of fluid flow in constricted tubes and ducts using body-fitted non-staggered grids," *Int. J. Numer. Meth. Fluids*, vol. 15, pp. 895–923, 1992.

[32] C. Bertolotti and V. Deplano, "Three-dimensional numerical simulations of flow through a stenosed coronary bypass," *J. Biomech.*, vol. 33, pp. 1011–1022, 2000.

[33] A. S. Dvinsky and M. Ojha, "Simulation of three-dimensional pulsatile flow through an asymmetric stenosis," *J. Biomech.*, vol. 32, pp. 138–142, 1994.

[34] Q. Long, X. Y. Xu, K. V. Ramnarine, and P. Hoskins, "Numerical investigation

of physiologically realistic pulsatile flow through arterial stenosis," *J. Biomech.*, vol. 34, pp. 1229–1242, 2001.

[35] S. J. Sherwin and H. M. Blackburn, "Three-dimensional instabilities and transition of steady and pulsatile axisymmetric stenotic flows," *J. Fluid Mech.*, vol. 533, pp. 297–327, 2005.

[36] H. M. Blackburn and S. J. Sherwin, "Instability modes and transition of pulsatile stenotic flow: pulse-period dependence," *J. Fluid Mech.*, vol. 573, pp. 57–88, 2007.

[37] D. E. Mann and J. M. Tarbell, "Flow of non-Newtonian blood analog fluids in rigid curved and straight artery models," *Biorheology*, vol. 27 (5), pp. 711–733, 1990.

[38] W. M. Phillips and S. Deutsch, "Toward a constitutive equation for blood," *Biorheology*, vol. 12 (6), pp. 383–389, 1975.

[39] F. M. Box, R. J. van der Geest, M. C. Rutten, and J. H. Reiber, "The influence of flow, vessel diameter, and non-newtonian blood viscosity on the wall shear stress in a carotid bifurcation model for unsteady flow," *Invest. Radiol.*, vol. 40, pp. 277–294, 2005.

[40] J. Boyd, J. M. Buick, and S. Green, "Analysis of the Casson and Carreau-Yasuda non-Newtonian blood models in steady and oscillatory flows using the lattice Boltzmann method," *Phys. Fluids*, vol. 19, p. 093103, 2007.

[41] H. W. Choi and A. I. Barakat, "Numerical study of the impact of non-Newtonian blood behavior on flow over a two-dimensional backward facing step," *Biorheology*, vol. 42, pp. 493–509, 2005.

[42] P. J. Carreau, "Rheological equation from molecular network theories," *J. Rheology*, vol. 16 (1), pp. 99–127, 1972.

[43] M. Nakamura and T. Sawada, "Numerical study on the flow of a non-Newtonian fluid through an axisymmetric stenosis," *ASME J. Biomech. Eng.*, vol. 110 (2), pp. 137–143, 1988.

[44] T. Ishikawa, L. F. R. Guimaraes, S. Oshima, and R. Yamane, "Effect of non-Newtonian property of blood on flow through a stenosed tube," *Fluid Dyn. Res.*, vol. 22, p. 251, 1998.

[45] P. L. Easthope and D. E. Brooks, "A comparison of rheological constitutive functions for whole human blood," *Biorheology*, vol. 17 (3), pp. 235–247, 1980.

[46] F. J. Walburn and D. J. Schneck, "A constitutive equation for whole human blood," *Biorheology*, vol. 13 (3), pp. 201–210, 1976.

[47] J. Hron, J. Malek, and S. Turek, "A numerical investigation of flows shear-thinning fluids with applications to blood rheology," *Int. J. Numer. Meth. Fluids*, vol. 32 (7), pp. 863–879, 2000.

[48] W. P. Jones and M. Wille, "Large-eddy simulation of a plane jet in a cross-flow," *Int. J. Heat Fluid Flow*, vol. 17 (3), pp. 296–306, 1996.

[49] W. P. Jones, F. di Mare, and A. J. Marquis, *LES-BOFFIN: User's Guide*. Technical Memorandum, Imperial College London, London, UK, 2002.

[50] G. Grotzbach, "Spatial resolution requirements for direct numerical simulations of the Rayleigh-Bernard convection," *J. Comp. Phys.*, vol. 49 (2), pp. 241–264, 1983.

[51] A. N. Kolmogorov, "Dissipation of energy in locally isotropic turbulence," *Dokl. Akad. Nauk SSSR*, vol. 32, pp. 16–18, 1941.

[52] H. Tennekes and J. L. Lumley, *A First Course in Turbulence*. The MIT Press, 1972.

[53] Y. Morinishi, T. S. Lund, O. V. Vasilyev, and P. Moin, "Fully conservative higher order finite difference schemes for incompressible flow," *J. Comp. Phys.*, vol. 143 (1), pp. 90–124, 1998.

[54] D. S. Kershaw, "The incomplete Cholesky-Conjugate gradient method for the iterative solution of systems," *J. Comp. Phys.*, vol. 26 (1), pp. 43–65, 1978.

[55] C. M. Rhie and W. L. Chow, "Numerical study of the turbulent flow past an airfoil with trailing edge separation," *AIAA J.*, vol. 21 (11), pp. 1525–1532, 1983.

[56] A. Hossain, "Large-eddy simulation of physiological pulsatile flow through arterial stenosis," Master's thesis, University of Manitoba, May 2012.

[57] J. R. Womersley, "Method for the calculation of velocity, rate of flow and viscous drag in arteris when the pressure gradient is known," *J. Physiol.*, vol. 155, pp. 553–563, 1955.

[58] R. Mittal, S. P. Simmons, and F. Najjar, "Numerical study of pulsatile flow in a constricted channel," *J. Fluid Mech.*, vol. 485, pp. 337–378, 2003.

[59] A. K. M. F. Hussain and W. C. Reynolds, "The mechanics of an organized wave in turbulent shear flow," *J. Fluid Mech.*, vol. 41 12), pp. 241–258, 1970.

[60] G. R. Andrews, *Foundations of Multithreaded, Parallel, and Distributed Programming*. Addison-Wesley, Reading, MA, 2000.

[61] J. B. Dennis and E. Van Horn, "Programming semantics for multiprogrammed computations," *Comm. ACM*, vol. 9 (3), pp. 143–155, 1966.

[62] P. C. Lu, D. R. Gross, and H. C. Hwang, "Intravascular pressure and velocity fluctuations in pulmonic arterial stenosis," *J. Biomech.*, vol. 13 (3), pp. 291–300, 1980.

[63] Y. C. Fung, *Biomechanics: Circulation.* 2nd edition, Springer, 1997.

[64] S. A. Berger and L. D. Jou, "Flows in stenotic vessels," *Annu. Rev. Fluid Mech.*, vol. 32, pp. 347–382, 2000.

[65] L. H. Back, Y. Cho, D. Crawford, and R. Cuffel, "Effect of mild atherosclerosis on low resistance in a coronary artery casting of man," *ASME J. Biomech. Eng.*, vol. 106, pp. 48–53, 1984.